REPORT DOCUMENTATION PAGE	Form Approved OMB NO. 0704-0188

1. AGENCY USE ONLY (Leave Blank)	2. REPORT DATE 31 Aug 06	3. REPORT TYPE AND DATES COVERED Final report: (1 Sep 05 - 31 May 06)
4. TITLE AND SUBTITLE Innovative Mechanism-Based Textile Composite Damage Modeling Basing on a Nonlinear Fiber Model and Enhanced Homogenization Method		5. FUNDING NUMBERS W911NF-05-1-0501
6. AUTHOR(S) Zheng-Dong Ma		
7. PERFORMING ORGANIZATION NAME(S) AND ADDRESS(ES) Department of Mechanical Engineering, University of Michigan 2250 G.G. Brown 2350 Hayward, Ann Arbor, MI 48109-2125		8. PERFORMING ORGANIZATION REPORT NUMBER F013433
9. SPONSORING / MONITORING AGENCY NAME(S) AND ADDRESS(ES) U. S. Army Research Office P.O. Box 12211 Research Triangle Park, NC 27709-2211		10. SPONSORING / MONITORING AGENCY REPORT NUMBER 48796.1-EG-II

11. SUPPLEMENTARY NOTES
The views, opinions and/or findings contained in this report are those of the author(s) and should not be construed as an official Department of the Army position, policy or decision, unless so designated by other documentation.

12 a. DISTRIBUTION / AVAILABILITY STATEMENT	12 b. DISTRIBUTION CODE
Approved for public release; distribution unlimited.	.

13. ABSTRACT (Maximum 200 words)

The ultimate goal of proposed research is to develop a new advanced simulation and designing tool of textiles and textile-based composites for developing lighter, more durable and affordable composite structures in military and commercial applications. In the current program, we have developed and integrated the following two new capabilities to our simulation and design system:

1. Extended nonlinear fiber model for simulating general textile fabrics and textile composite materials.
2. A high fidelity meso-structural model for textile composites.

We have extended our nonlinear fiber model to general three-dimensional fabric system with arbitrary configuration and with interactions with other fibers and materials in the composite for simulating a practical textile composite. The new model accounts for geometry nonlinearity and arbitrary large deformation of fibers, fiber-to-fiber contacts, and fiber-to-other material contacts in a textile composite. This results in a unique capability for simulating textile composites, especially for more accurate damage assessment. The new capability will be further extended and integrated with the other advanced capabilities being developed for designing truly optimum textile composites for military and commercial applications.

14. SUBJECT TERMS			15. NUMBER OF PAGES
Textile Composites, Lightweight Structure Technologies, Tactical and Support Vehicle Fleets, Mechanism-based Damage Model, Textile Fabrics.			46
			16. PRICE CODE
17. SECURITY CLASSIFICATION OR REPORT **UNCLASSIFIED**	18. SECURITY CLASSIFICATION ON THIS PAGE **UNCLASSIFIED**	19. SECURITY CLASSIFICATION OF ABSTRACT **UNCLASSIFIED**	20. LIMITATION OF ABSTRACT **UL**

NSN 7540-01-280-5500

Standard Form 298 (Rev.2-89)
Prescribed by ANSI Std. 239-18
298-102

Enclosure 1

The University of Michigan

1002 W.E. Lay Automotive Laboratory
1231 Beal Avenue
Ann Arbor, MI 48109-2133

To: US Army Research Office
P.O. Box 12211
Research Triangle Park
RTP, NC 27709-2211

Phone #: (919) 549-4397

From: Dr. Zheng-Dong Ma

Subject:	Contract No:	W911NF-05-1-0501
	UM No:	F013433 (DRDA Number: 05-4171)
	Title:	Innovative Mechanism-Based Textile Composite Damage Modeling Basing on a Nonlinear Fiber Model and Enhanced Homogenization Method
	Report Type:	Technical Report
	Reporting Period:	09/01/05 to 05/31/06

Attention: Dr. Bruce LaMattina, Branch Chief, Solid Mechanics (bruce.lamattina@us.army.mil)

Dear Dr. LaMattina:

Enclosed is the final technical report for the above referenced contract. Please feel free to contact me if you have any comments and suggestions or require any additional information.

Sincerely yours,

Zheng-Dong Ma, Ph.D.
Research Scientist

Department of Mechanical Engineering
University of Michigan
Ann Arbor, MI 48109

Email: mazd@umich.edu
Phone: (734) 764-8481
Fax: (734) 764-4256

cc: Susan Clair (sclair@umich.edu)
Kathy DeWitt (dewitt@mail.drda.umich.edu)
Farzad Rostam-Abadi (rostamf@tacom.army.mil)

Innovative Mechanism-Based Textile Composite Damage Modeling Basing on a Nonlinear Fiber Model and Enhanced Homogenization Method[1]

Table of Content

[1] The reported contents have been pre-communicated with Mr. Farzad Rostam-Abadi at US Army RDECOM.

1 EXECUTIVE SUMMARY

The ultimate goal of proposed research is to develop a new advanced simulation and designing tool of textiles and textile-based composites for developing lighter, more durable and affordable composite structures in military and commercial applications. The mechanism-based damage model developed in this research enables predicting validated physics of failure characterization of textile-based composites so that eliminates conservative design penalties. Different from the existent composite models, the new model addresses issues related to different local damage mechanisms based on "meso-structural" behaviors of fibers with the use of a truly nonlinear fiber model, high-fidelity fiber-to-fiber, fiber-to-other material interaction models, and an enhanced homogenization method. The developed model can greatly enhance accuracy and efficiency of simulation and design for textile-based composite structures, such as for advanced composite armors, under various static and dynamic loading conditions, while further extension can also include ballistic and blast loading conditions. The developed innovative textile mechanics model and simulation and designing tool will also find important applications in protective clothing and parachute applications for protecting individual soldiers.

In the current program of the proposed research, we have developed and integrated the following two new capabilities to our simulation and design system:

1. Extended nonlinear fiber model for simulating general textile fabrics and textile composite materials.
2. A high fidelity meso-structural model for textile composites.

We have extended our nonlinear fiber model to general three-dimensional fabric system with arbitrary configuration and with interactions with other fibers and materials in the composite for simulating a practical textile composite. The new model accounts for geometry nonlinearity and arbitrary large deformation of fibers, fiber-to-fiber contacts, and fiber-to-other material contacts in a textile composite. This results in a unique capability for simulating textile composites, especially for more accurate damage assessment. The new capability will be further extended and integrated with the other advanced capabilities being developed for designing truly optimum textile composites for military and commercial applications.

***Keywords*:**

Textile Composites, Lightweight Structure Technologies, Future Combat Systems, Tactical and Support Vehicle Fleets, Mechanism-based Damage Model, Textile Fabrics.

2 BACKGROUND

One of Army research goals within the next ten years is to develop design and analytical tools that can predict the impact damage and the corresponding post-impact performance and strength of the composite structures. Another special interest the Army has is to develop new experimental and analytical methodologies for textile materials that are used for protective clothing and parachutes for the soldiers. The objective of proposed research is to develop advanced simulation and designing tools for textiles and textile-based composites for the need to design lighter, more durable and affordable composite structures for the Future Combat Systems (FCS) and other military applications. The mechanism-based damage model proposed in this research will enable validated physics of failure characterization to eliminate conservative design penalties. Different from existing models, the new model developed in this program will address issues of different local damage mechanisms based on “meso-structural” behaviors of fibers, truly nonlinear fiber model, high-fidelity fiber-matrix interaction model, and an enhanced homogenization method. The developed model can greatly enhance simulation and design of the textile composite structures in ground vehicles under various loading conditions, including ballistic and blast impacts. The innovative textile mechanics model and simulation and designing tools will also find important applications in protective clothing and parachutes for the soldiers.

We are accumulating advanced and unique analytical and design capabilities for developing innovative composite structures for Army future combat and tactical vehicles. The new capabilities, developed and being developed, include:

1. Function-oriented material design (FOMD) with a multi-domain, multi-step, multi-material topology optimization process.

2. Multi-scale modeling and homogenization method.

3. Fabrics mechanics-based damage prediction.

4. Truly nonlinear fiber model, which accounts for arbitrary large-deformation of elastic fiber, uneven tension distribution along the fiber, fiber-fiber or fiber-matrix interaction for high-fidelity prediction of fiber behavior in a composite material.

5. Fiber arrangement optimization in composite materials.

6. Advanced structural analysis capabilities for durability, NVH, crashworthiness, ballistic and blast simulations.

These advanced capabilities are being integrated into a unique simulation and design platform, which can be used for designing and evaluating innovative composite materials and structures in future vehicle systems. Following are brief summaries of the methodologies being developed.

2.1 Advanced Textile Composite Damage Modeling

Textile-based composites are outstanding candidates for lightweight vehicle structural materials. Textile fabrics are also widely used in soldier systems, such as protective clothing, parachutes, and shelters. Predictions of elastic properties of textile composites can now be found in many literatures. However, the non-linear behaviors and the damage mechanism of textiles and textile-based composites have not been fully understood due to the complex geometry effects and anisotropic non-linear properties of the associated meso-structures. As a result, damage modeling of textile composites is still an active research area. There are various models for textile composite damage simulation, which either greatly simplify the material behaviors, or are too complicated and inefficient in aspect of practical usage. In the previous models, the textile composites are modeled as materials similar to homogeneous materials. Especially in damage modeling, the detailed damage sequences and mechanisms are not actually accounted for. In our proposed model, textile composites will have detailed texture and “meso-structures” with the consideration of essential fiber nonlinear characteristics, which can be used to predict the meso-structural behaviors of the textile and textile composites, including delaminations and local damages. An enhanced homogenization method will be then developed to include this textile composite model for the macro-structural analysis with the needed computational efficiency. This results in a multi-scale modeling process, which can be used to predict both “global” and “local” behaviors of the composite. The major focus is to develop an advanced fiber-matrix model for the textile composite. This model will base on the local mechanical behavior of the material and local damage mechanism, so that high fidelity damage prediction can be obtained. The proposed multi-scale model will also be highly efficient for simulation and design of composite due to the enhanced homogenization method and advanced computational algorithms to be developed. Figure 1 summarizes the scope of work for the research at The University of Michigan related to textile composites.

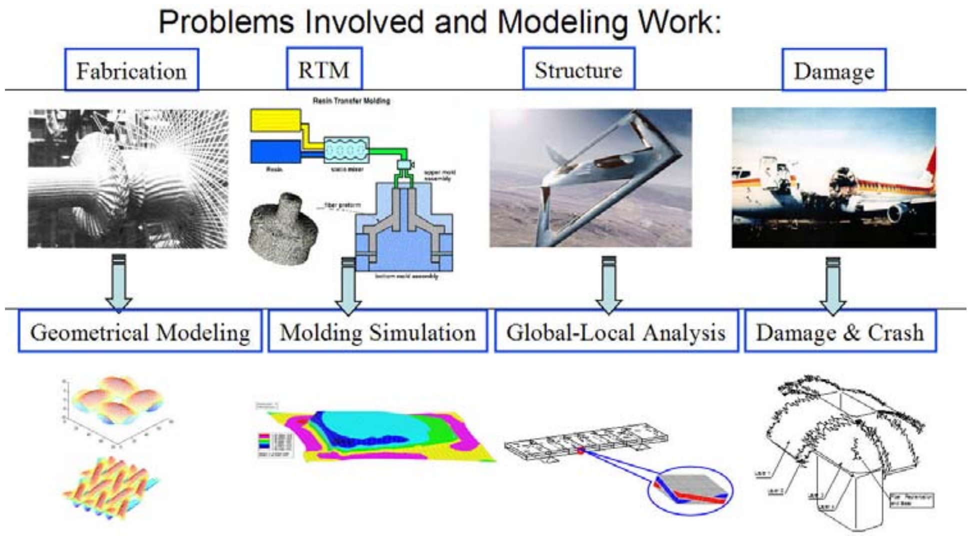

Figure 1. Scope of work of the research at U of M related to textile composites

2.2 Simulation and Design Capabilities to be Integrated

2.2.1 Function-oriented material design (FOMD)

We have developed an award-winning advanced CAE tool, called FOMD (Function-Oriented Material Design) [1-14], which employs a multi-domain, multi-step and multi-material topology optimization approach. Our FOMD technology has received a best paper award in 2003 from the ASME Design Engineering Division [1]. FOMD has been developed as a commercial-grade CAE tool for designing advanced and high-performance structures and materials. Figure 2 illustrates example graphic user interfaces of a FOMD-*Blast* simulation and design system, which is being developed for designing advanced blast-protective composites [14]. As shown in Fig. 2, this software system includes: 1) explosive modeling, 2) soil modeling for landmine-soil interaction, 3) geometry modeling of vehicle structure and occupants, 4) blast prediction, which will predict both blast pressure and fragment penetrations on the composite, 5) composite layout, which includes raw material selection and basic material configuration, 6) optimal design based on the FOMD and topology optimization. This software system will be continuously extended to include more advanced modeling and simulation capabilities and post-processes that will finalize the designs for prototyping and mass production.

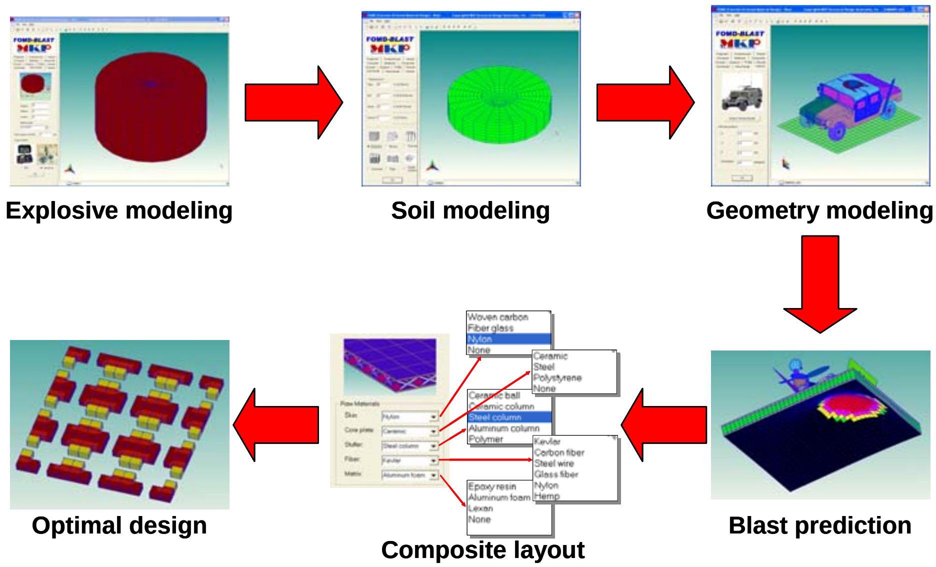

Figure 2. Proposed simulation and design process

2.2.2 Multi-scale modeling and homogenization method

Figure 3 illustrates fundamental idea of the multi-scale modeling. As shown in Fig. 3, a completed modeling process should starts from the micro-level with the consideration of micro-structural behavior of the composite material. For example, detailed micro-structure of a fiber or thread can be considered at this stage. Then effective material properties of the fiber or thread at the meso-level can be estimated through a homogenization process from the micro-level to the meso-level. Next, a higher level homogenization process can be employed, which estimates effective material properties of, for example, a cut-off piece of the composite, from the meso-level to the macro-level. Finally, a structural analysis can be conducted at the macro-level without considering composite details at the micro- and meso- levels. This micro-meso-macro modeling process makes the composite analysis highly efficient and effective without loosing any detail of the composite at the meso- and micro levels. In next step, we will develop and implement a new generated homogenization method, which will suit the needs described here.

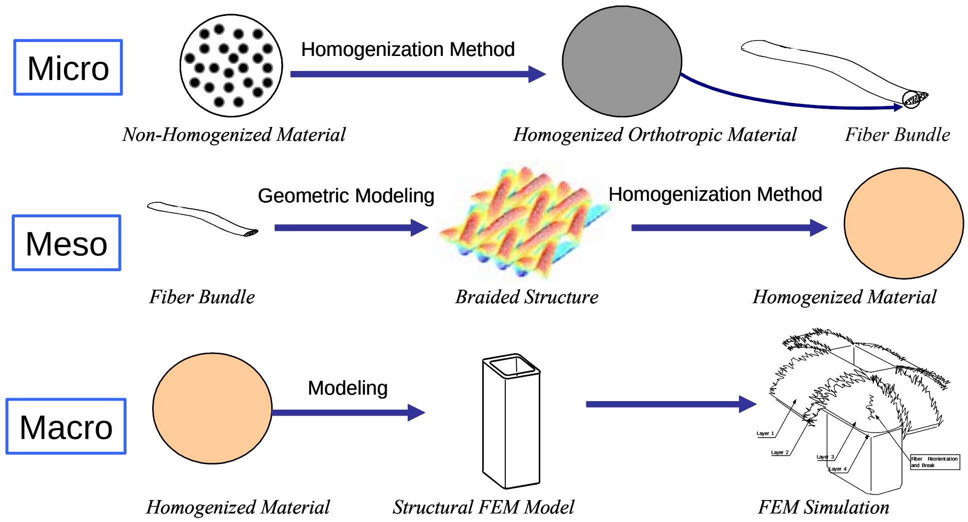

Figure 3. Hierarchical modeling at micro-, meso-, and macro-levels

2.2.3 Fabrics mechanics-based damage prediction

An advanced model for fabrics has been developed at the University of Michigan with the assumption of small fiber deformation and linear geometry [15]. This model is unique compared to the state-of-art models in several aspects: 1) it is based on physical behaviors of fiber yarns instead of assumptions; 2) it is numerically efficient; 3) it enables automatic modeling for textile composites with a few design parameters; 4) it can be modified to use in textile modeling. Figure 4 illustrates some example geometrical modeling works conducted at the U of M with a traditional finite element approach [16].

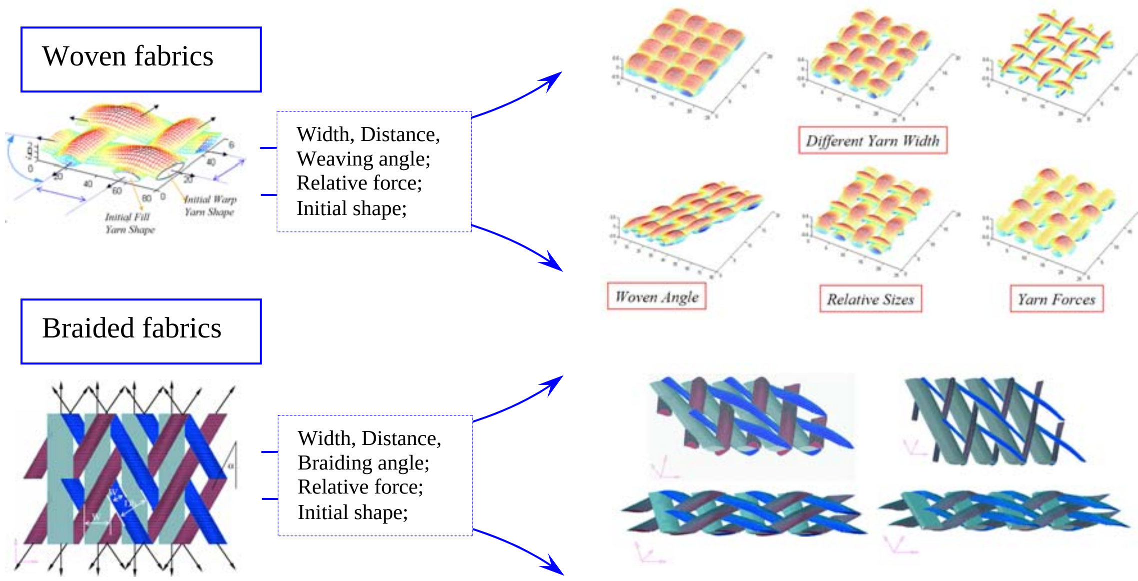

Figure 4. Fabrics mechanics and geometrical modeling [2]

There are different mechanisms in textile composites damage process. For example, the damage of woven composites will include the delamination of fiber tows, and the sliding between the separated tows after the initial damage. Most current models cannot address these damage mechanisms. In the framework of our general nonlinear multi-scale model, this kind of mechanism can be easily considered, and the influences of different damage mechanism on overall material performances can be investigated in details. The freedom provided will also include the possibility to consider additional new damage mechanisms observed in testing processes.

3 TECHNICAL OBJECTIVES AND PROPOSED TASKS

3.1 Technical Objectives of the Overall Research

The ultimate goal of the proposed research is to develop a comprehensive and advanced simulation and designing tool for textiles and textile-based composites for the need of designing lighter, more durable and affordable composite structures for future military applications. The mechanism-based damage model proposed in this research will enable validated physics of failure characterization to eliminate conservative design penalties. The new model developed in this program will address issues of different local damage mechanisms based on "meso-structural" behaviors of the fibers. We are proposing to develop and integrate the following new capabilities to our simulation and design system:

1. Innovative mechanical model for textile fabrics.
2. Nonlinear multi-scale modeling for textile composites.
3. Mechanism-based damage modeling for high-fidelity prediction.

Detailed technical objectives of the overall research are enumerated as follows:

1. Extend our nonlinear fiber model for simulating general textile fabrics and composite materials
2. Develop high fidelity meso-structural model of textile composites
3. Develop advanced homogenization theory for micro-meso-macro modeling of textile composites
4. Develop advanced mechanism-based damage theory for textile composites
5. Develop effective and efficient numerical tools for analysis and design of textile composites
6. Conduct proof-of-concept through prototyping and example applications

In the current program, we proposed to focus on the first two tasks as a preliminary and feasibility study for the further developments in this research.

3.2 Proposed Tasks in the Current Program

The following tasks were proposed to be carried out in the current phase of the research program:

3.2.1 Task I – Extend our nonlinear fiber model for simulating general textile fabrics and textile composite materials

In this task, we proposed to extend our nonlinear fiber model to general three-dimensional fabric system with various configurations for simulating practical textile fabrics and composite materials. The formulation will account for geometry nonlinearity and arbitrary large deformation of the textile fabrics. This will result in a unique capability for simulating textile composite materials, especially for the damage assessment.

3.2.2 Task II – Develop a high fidelity meso-structural model for textile composites

In this task, we proposed to develop a high-fidelity meso-structural model for general textile composite, which will include fiber/fabrics and filling/matrix material. This meso-structural model would allow us to conduct a detailed localized analysis for the meso-behaviors of the composite, which include nonlinear deformation and strength of individual fibers in the composite.

4 MAJOR RESULTS

4.1 Development of the New Nonlinear Fiber Model

We have developed a new capability to simulate a truly nonlinear and large deformation fiber system based on an efficient and advanced formulation of three-dimensional fiber systems. [15] The new fiber model is in a very compact form, resulted from employing proper coordinate systems and state variables. It accounts for geometry nonlinearity, extensibility of the fiber, tension variation along the fiber, tension-dependent mechanical properties of the fiber, and other nonlinear effects in such fiber system undergoing arbitrary large deformation.

4.1.1 Basic equations

4.1.1.1 State equations

Figure 5-a illustrates a general thread member taken out from a fabric system with the adoption of a curvilinear coordinate system. Figure 5-b illustrates the equilibrium of an infinitesimal element cut out from the thread at point P. As shown in Fig. 5-a, for an arbitrary material point P on the thread, vector $\mathbf{r} = \{x,\ y,\ z\}^T$ represents the position of P in the global coordinate system, O-XYZ. In general, $\mathbf{r}$ is a function of space variable and time variable. For deriving the thread model with an arbitrary initial shape and potential large deformation, we adopt a local coordinate s, which represents undeformed arc-length $\overset{\frown}{oP}$ measured from the left end of the thread (namely point o in Fig. 5) to the material point P along the axial curve of the thread.

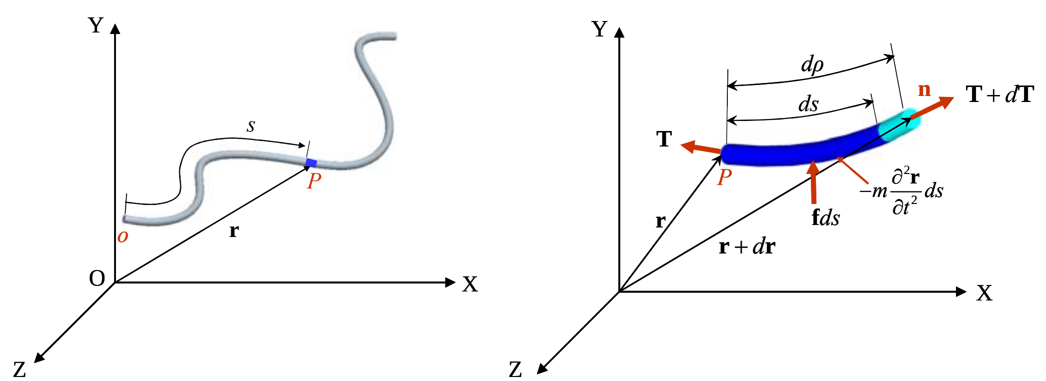

a) A thread member **b) Equilibrium of an infinitesimal element**

Figure 5. Modeling of a nonlinear thread member

Figure 5-b illustrates the equilibrium of the infinitesimal element cut out from the thread at point *P*. Here, ds denotes the undeformed arc length of the infinitesimal element, $d\rho$ denotes the elongated arc length of the same element after fiber deformation due to the tension and external force applied on the element, $\mathbf{T} = \left\{T_x,\ T_y,\ T_z\right\}^T$ denotes the tension vector acting on the point *P*, $\mathbf{f} = \left\{f_x, f_y, f_z\right\}^T$ denotes the external force/per length acting on the element, and $-m\dfrac{\partial^2 \mathbf{r}}{\partial t^2}$ is the inertial force/ per length, where *m* denotes density of the thread, and $\mathbf{a} = \dfrac{\partial^2 \mathbf{r}}{\partial t^2}$ is the acceleration vector of the thread element. It is assumed that the external force is non-following with a fixed coordinate *s* at the arc-length coordinate system, and its amplitude and direction are independent of the elongation of the thread, namely we have $\mathbf{f} = \mathbf{f}(s,t)$. Note that a following-type force can also be considered and corresponding formulation can be obtained using a similar approach described in this report.

From Fig. 5-b, the equilibrium of the forces acting on the thread element can be obtained as

$$\frac{\partial \mathbf{T}}{\partial s} - m\frac{\partial^2 \mathbf{r}}{\partial t^2} + \mathbf{f} = 0\,, \tag{1}$$

Assuming that *T* is the magnitude of the tension vector **T,** and **n** is the unit direction vector of **T**, we have,

$$\mathbf{T} = T\mathbf{n} \tag{2}$$

where *T* can be calculated using

$$T = \sqrt{\mathbf{T}^T\mathbf{T}}\,. \tag{3}$$

From Fig. 5-b, the direction vector, **n**, can be calculated as

$$\mathbf{n} = \frac{\partial \mathbf{r}}{\partial \rho}\,, \tag{4}$$

here, elongation of thread element has been considered in Eq. (4), this results in a formulation that can account for extensibility of the fiber or thread.

To simplify the problem, let us consider that the thread member is made of a linear elastic material, which obeys a constitution law:

$$T = EA\left(\frac{d\rho}{ds} - 1\right), \tag{5}$$

which implies that the tension force T is determined by tensile modulus, E, thread cross-section area, A, and strain (elongation/length), namely $\left(d\rho - ds\right)/ds$. From Eq. (5), we can obtain

$$\frac{ds}{d\rho} = \frac{EA}{EA + T} \tag{6}$$

Substituting Eq. (4) into Eq. (2) and using derivative chain rule obtains

$$\mathbf{T} = T\frac{\partial \mathbf{r}}{\partial \rho} = T\frac{\partial \mathbf{r}}{\partial s}\frac{ds}{d\rho} \tag{7}$$

Substituting Eq. (6) into Eq. (7) obtains

$$\mathbf{T} = \hat{T}\frac{\partial \mathbf{r}}{\partial s}, \tag{8}$$

where

$$\hat{T} = \frac{EA \cdot T}{EA + T} \tag{9}$$

is called generalized tension in this report, which has the same dimension as the tension. Note that for an inextensible thread, we have $EA \to \infty$ and therefore $\hat{T} \to T$.

Substituting Eq. (8) into Eq. (1), the governing equation for the thread member can be obtained as

$$-\frac{\partial}{\partial s}\left(\hat{T}\frac{\partial \mathbf{r}}{\partial s}\right) + m\frac{\partial^2 \mathbf{r}}{\partial t^2} = \mathbf{f}. \tag{10}$$

It is seen that the equation of motion becomes very simple, which is resulted from the introduction of a new generalized tension variable, $\hat{T}$, and the local arc-length coordinate.

For a static equilibrium problem, assuming that $\mathbf{f} = \mathbf{f}_s(s)$ is static force acting on the thread, Eq. (10) can be reduced as

$$-\frac{d}{ds}\left(\hat{T}\frac{d\mathbf{r}}{ds}\right)=\mathbf{f}_s\,, \tag{11}$$

where $\hat{T}=\hat{T}(\mathbf{r})$ is a function of the thread configuration through the relationship defined by Eqs. (9), (5), and $\frac{d\rho}{ds}=\sqrt{\left(\frac{d\mathbf{r}}{ds}\right)^T\left(\frac{d\mathbf{r}}{ds}\right)}$.

Vibration problem of the thread is usually considered about the static equilibrium configuration. Assuming that $\mathbf{f}_d=\mathbf{f}_d(s,t)$ is a dynamic force acting on the thread in addition to the static force $\mathbf{f}_s$, namely we have $\mathbf{f}=\mathbf{f}_s+\mathbf{f}_d$, then Eq. (10) can be rewritten as

$$-\frac{\partial}{\partial s}\left(\hat{T}(\mathbf{r})\frac{\partial\overline{\mathbf{r}}}{\partial s}\right)+m\frac{\partial^2\overline{\mathbf{r}}}{\partial t^2}=\mathbf{f}_d\,, \tag{12}$$

where $\overline{\mathbf{r}}$ denotes the dynamic deformation from the static equilibrium position, and $\mathbf{r}=\overline{\mathbf{r}}+\mathbf{r}_s$, where $\mathbf{r}_s$ is the solution obtained from the static equilibrium problem Eq. (11). In Eq. (12), we assumed the external force is independent of the tread deformation. However, this assumption can be relaxed when necessary for the corresponding applications. Note that if the vibration amplitude is sufficiently small, then Eq. (12) can be simplified into its corresponding linearized form, which will be discussed in the next section.

4.1.1.2 Incremental form

Equation (11) results in a two-point nonlinear boundary value problem. To solve it, an incremental form of the thread model is obtained by assuming $\mathbf{r}=\mathbf{r}_0+\Delta\mathbf{r}$, $\hat{T}=\hat{T}_0+\Delta\hat{T}$, and $\mathbf{f}_s=\mathbf{f}_0+\Delta\mathbf{f}$, where $\mathbf{r}_0$ is an approximate solution of Equation (11) obtained from a prior iteration with associated tension measure $\hat{T}_0$ and loading $\mathbf{f}_0$. Using an important relationship:

$$\Delta\hat{T}\frac{d\mathbf{r}}{ds}=\hat{T}\frac{EA}{T^3}\mathbf{T}\mathbf{T}^T\left(\frac{d\Delta\mathbf{r}}{ds}\right), \tag{13}$$

the incremental form of Eq. (11) can be obtained as

$$-\frac{d}{ds}\left(\mathbf{B}\frac{d\Delta\mathbf{r}}{ds}\right)-\mathbf{G}\Delta\mathbf{r}=\mathbf{e}\,, \tag{14}$$

where $\mathbf{B}$ is called (linearized) stiffness matrix of the thread,

$$\mathbf{B} = \hat{T}_0\left(\mathbf{I} + \frac{EA}{T_0^3}\mathbf{T}_0\mathbf{T}_0^T\right), \tag{15}$$

$\mathbf{G}$ is the tangent matrix of the external force,

$$\mathbf{G} = \left.\frac{d\mathbf{f}}{d\mathbf{r}}\right|_{\mathbf{r}=\mathbf{r}_0}, \tag{16}$$

and $\mathbf{e}$ is the residual vector obtained at the last iteration step,

$$\mathbf{e} = \mathbf{f}_0 + \frac{d}{ds}\left(\hat{T}_0\frac{d\mathbf{r}_0}{ds}\right). \tag{17}$$

Stiffness matrix $\mathbf{B}$ in Eq. (16) is a function of the previous tension, $\mathbf{T}_0$, where $\mathbf{T}_0$ denotes the tension vector $\mathbf{T}$ obtained at the previous iteration step, and $\hat{T}_0$ is the generalized tension obtained at the previous iteration step, $\hat{T}_0 = \frac{EA \cdot T_0}{EA + T_0}$, where $T_0 = |\mathbf{T}_0|$. Tangent matrix $\mathbf{G}$ in Eq. (17) is empty when $\mathbf{f}$ is independent of the position vector $\mathbf{r}$, (for example, if only self weight of the thread is considered), and it becomes non-empty when $\mathbf{f}$ is a function of the position vector $\mathbf{r}$, (for example, if the thread is in contact with other deformable objects.)

Equation (15) is linear in terms of $\Delta\mathbf{r}$. Solving Eq. (15) for $\Delta\mathbf{r}$, an updated solution for $\mathbf{r}$ can be obtained as

$$\mathbf{r} = \mathbf{r}_0 + \Delta\mathbf{r}. \tag{18}$$

Using the updated $\mathbf{r}$, the updated tension vector $\mathbf{T}$ can be obtained as

$$\mathbf{T} = \hat{T}\frac{d\mathbf{r}}{ds}, \tag{19}$$

where

$$\hat{T} = \frac{EA \cdot T}{EA + T} \text{ and } T = EA\left(\sqrt{\left(\frac{d\mathbf{r}}{ds}\right)^T\left(\frac{d\mathbf{r}}{ds}\right)} - 1\right). \tag{20}$$

Substituting Eqs. (20) and (21) into Eq. (16) the stiffness matrix $\mathbf{B}$ can be then updated, which can be then used for next iteration.

Incremental form of the vibration equation Eq. (12) can be obtained by extending the above formulation with added inertial term. As a result, we have

$$-\frac{\partial}{\partial s}\left(\mathbf{B}\frac{\partial \Delta \mathbf{r}}{\partial s}\right)+m\frac{\partial^2 \Delta \mathbf{r}}{\partial t^2}=\mathbf{f}_d\,, \tag{21}$$

where $\mathbf{B}=\mathbf{B}(\mathbf{T}_0)$, $\mathbf{T}_0=\mathbf{T}(\mathbf{r}_0)$, and $\mathbf{T}_0$ and $\mathbf{r}_0$ satisfy the static equilibrium equation:

$$\frac{d}{ds}\left(\hat{T}_0\frac{d\mathbf{r}_0}{ds}\right)+\mathbf{f}_s=0\,. \tag{22}$$

It is assumed here that vibration amplitude is sufficiently small, so the stiffness matrix $\mathbf{B}$ needs not be updated during the vibration analysis. Therefore, Eq. (21) becomes a linear equation for solving $\Delta\mathbf{r}$. Note that the stiffness matrix $\mathbf{B}$ in Eqs. (21) is, however, not constant with respect to the arc-length coordinate, and in general we have $\mathbf{B}=\mathbf{B}(s)$, which is determined by solving the static equilibrium equation (22).

4.1.1.3 Weak form and finite element discretization

The weak form of Equation (14) is

$$\int_0^L \frac{d\delta\mathbf{w}^T}{ds}\mathbf{B}\frac{d\Delta\mathbf{r}}{ds}ds-\int_0^L \delta\mathbf{w}^T\mathbf{G}\Delta\mathbf{r}ds=\int_0^L \delta\mathbf{w}^T\mathbf{f}_0 ds-\int_0^L \hat{T}_0\frac{d\delta\mathbf{w}^T}{ds}\frac{d\mathbf{r}_0}{ds}ds \tag{23}$$

where $\delta\mathbf{w}$ denotes virtual displacement, and L is the total length of the thread.

A finite element method can be then employed to discretize Eq. (23). In general, assuming that the thread shown in Fig. 1 is divided into n_{el} finite elements, each element has two nodes at the left and right ends with coordinates, s_e and s_{e+1}, in the arc-length coordinate system (where $e=1,2,\cdots,n_{el}$). Also assuming that $\mathbf{\Phi}=\mathbf{\Phi}(s)$ ($s \in \left[s_e, s_{e+1}\right]$) is the selected shape function matrix for the *e*-th element, then for element *e* we have

$$\Delta\mathbf{r}=\mathbf{\Phi}\mathbf{u}^e\,, \tag{24}$$

where, $\mathbf{u}^e = \left\{\Delta\mathbf{r}_e^T, \Delta\mathbf{r}_{e+1}^T\right\}^{\mathrm{T}}$ is the vector of nodal variable perturbations for the *e*-th element. Then the equilibrium equation for the *e*-th element becomes

$$\mathbf{k}_e\mathbf{u}^e = \mathbf{f}_e\,, \tag{25}$$

where

$$\mathbf{k}_e = \int_{s_e}^{s_{e+1}} \left(\boldsymbol{\Phi}_e^{'T}\mathbf{B}\boldsymbol{\Phi}_e^{'} - \boldsymbol{\Phi}_e^T\mathbf{G}\boldsymbol{\Phi}_e\right) ds\,, \tag{26}$$

$$\mathbf{f}_e = \int_{s_e}^{s_{e+1}} \boldsymbol{\Phi}_e^T \left[\mathbf{f}_0 + \frac{d}{ds}\left(\hat{T}_0 \frac{d\mathbf{r}_0}{ds}\right)\right] ds\,, \tag{27}$$

where $\boldsymbol{\Phi}_e^{'} = \dfrac{d\boldsymbol{\Phi}_e}{ds}$.

Upon assemble, the incremental equation for the residual becomes

$$\mathbf{KU} = \mathbf{F}\,, \tag{28}$$

where $\mathbf{U} = \left\{\Delta\mathbf{r}_1^T, \Delta\mathbf{r}_2^T, \cdots, \Delta\mathbf{r}_{n_{el}+1}^T\right\}^T$ is the global perturbation vector for the nodal variables, $\mathbf{K}$ is the global stiffness matrix, and $\mathbf{F}$ is the global residual vector,

$$\mathbf{K} = \mathop{\mathrm{A}}_{e=1}^{n_{el}}\left(\mathbf{k}_e\right) \text{ and } \mathbf{F} = \mathop{\mathrm{A}}_{e=1}^{n_{el}}\left(\mathbf{f}_e\right). \tag{29}$$

Solving Eq. (28) for $\Delta\mathbf{r}_e$ ($e = 1, 2, \cdots, n_{el}+1$), the nodal coordinate vector $\mathbf{r}_e$ can be updated as

$$\mathbf{r}_e = \mathbf{r}_{0e} + \Delta\mathbf{r}_e\,, \tag{30}$$

where $\mathbf{r}_{0e}$ is the nodal coordinate vector of element e obtained in the last step and ($e = 1, 2, \cdots, n_{el}+1$). Using the updated $\mathbf{r}_e$, the updated tension vector $\mathbf{T}$ for element e can be obtained as

$$\mathbf{T}_e = \hat{T}_e\boldsymbol{\Phi}_e^{'}\mathbf{u}_e\,, \tag{31}$$

where ($e = 1, 2, \cdots, n_{el}+1$), $\mathbf{u}_e = \left\{\mathbf{r}_e^T, \mathbf{r}_{e+1}^T\right\}^T$,

$$\hat{T}_e = \frac{EA \cdot T_e}{EA + T_e}, \text{ and } T_e = EA\left(\sqrt{\mathbf{u}_e^T \mathbf{\Phi}_e^{'T} \mathbf{\Phi}_e^{'} \mathbf{u}_e} - 1\right). \tag{32}$$

Using Eqs. (31) and (32), the stiffness matrix $\mathbf{B}_e$ for element *e* can be updated, as

$$\mathbf{B}_e = \hat{T}_e \left(\mathbf{I} + \frac{EA}{T_e^3} \mathbf{T}_e \mathbf{T}_e^T \right), \tag{33}$$

which can be then used for next iteration step.

The finite element equation for the vibration problem can be obtained as

$$\mathbf{KU} + \mathbf{M\ddot{U}} = \mathbf{F}_d \tag{34}$$

where **M** is the global mass matrix,

$$\mathbf{M} = \mathop{\mathrm{A}}_{e=1}^{n_{el}} \left(\mathbf{m}_e \right) \tag{35}$$

and

$$\mathbf{m}_e = \int_{s_e}^{s_{e+1}} m \mathbf{\Phi}_e^T \mathbf{\Phi}_e ds , \tag{36}$$

4.1.2 Numerical implementation

4.1.2.1 Finite element discretization with linear shape functions

With linear interpolation, the incremental elementary nodal displacement vector, $\mathbf{u}^i$, is assumed to have the following form:

$$\mathbf{u}^e = \left\{ \Delta \mathbf{r}_e^T, \Delta \mathbf{r}_{e+1}^T \right\}^{\mathrm{T}}, \tag{37}$$

where $\triangle \mathbf{r}_i = \left\{ \triangle x_i, \triangle y_i, \triangle z_i \right\}$ is the incremental nodal displacement vector for the *i*-th node. The shape function matrix, $\mathbf{\Phi}_e$, is then assumed to have the following form:

$$\mathbf{\Phi}_e = \begin{bmatrix} \phi_1 & 0 & 0 & \phi_2 & 0 & 0 \\ 0 & \phi_1 & 0 & 0 & \phi_2 & 0 \\ 0 & 0 & \phi_1 & 0 & 0 & \phi_2 \end{bmatrix}, \tag{38}$$

where,

$$\phi_1 = \frac{1}{d_i}\left(s_{i+1} - s\right),\ \ \phi_2 = \frac{1}{d_i}\left(s - s_i\right), \text{ and } d_i = s_{i+1} - s_i \text{ for } s \in [s_i, s_{i+1}] \tag{39}$$

4.1.2.2 Finite element discretization with second-order polynomials

With the second-order polynomial interpolation, nodal displacement, $\mathbf{u}^i$ is assumed to have the following form:

$$\mathbf{u}^e = \left\{\Delta\mathbf{r}_e^T, \Delta\mathbf{r}_{e+1/2}^T, \Delta\mathbf{r}_{e+1}^T\right\}^T, \tag{40}$$

where a mid-node with the incremental displacement, $\Delta\mathbf{r}_{i+1/2}^T = \left\{\triangle x_{i+1/2}, \triangle y_{i+1/2}, \triangle z_{i+1/2}\right\}^T$ is added in the second-order element. The shape function matrix, Φ, is then assumed to have the following form:

$$\mathbf{\Phi}_e = \begin{bmatrix} \phi_1 & 0 & 0 & \phi_2 & 0 & 0 & \phi_3 & 0 & 0 \\ 0 & \phi_1 & 0 & 0 & \phi_2 & 0 & 0 & \phi_3 & 0 \\ 0 & 0 & \phi_1 & 0 & 0 & \phi_2 & 0 & 0 & \phi_3 \end{bmatrix}, \tag{41}$$

where,

$$\phi_1 = 1 - \frac{3s}{L} + \frac{2s^2}{L^2},\ \ \phi_2 = \frac{4s}{L} - \frac{4s^2}{L^2},\ \ \phi_3 = -\frac{s}{L} + \frac{2s^2}{L^2}, \text{ for } s \in [0, L] \tag{42}$$

With the assumption that the external force is independent of fiber position (namely, **G** = 0), the element stiffness matrix can be expressed as

$$k_1^e = \int_0^L \Phi'^T \mathbf{B}\Phi' ds = \int_0^{\frac{L}{2}} \Phi'^T \mathbf{B}\Phi' ds + \int_{\frac{L}{2}}^L \Phi'^T \mathbf{B}\Phi' ds \tag{43}$$

For further numerical implementation, The matrix $\Phi'^T \mathbf{B}\Phi'$ in Eq. (28) is expanded below:

$$
\Phi^{'T}\mathbf{B}\Phi^{'}=\begin{bmatrix}
\phi_1^{'}b_{11}\phi_1^{'} & \phi_1^{'}b_{12}\phi_1^{'} & \phi_1^{'}b_{13}\phi_1^{'} & \phi_1^{'}b_{11}\phi_2^{'} & \phi_1^{'}b_{12}\phi_2^{'} & \phi_1^{'}b_{13}\phi_2^{'} & \phi_1^{'}b_{11}\phi_3^{'} & \phi_1^{'}b_{12}\phi_3^{'} & \phi_1^{'}b_{13}\phi_3^{'} \\
 & \phi_1^{'}b_{22}\phi_1^{'} & \phi_1^{'}b_{23}\phi_1^{'} & \phi_1^{'}b_{21}\phi_2^{'} & \phi_1^{'}b_{22}\phi_2^{'} & \phi_1^{'}b_{23}\phi_2^{'} & \phi_1^{'}b_{21}\phi_3^{'} & \phi_1^{'}b_{22}\phi_3^{'} & \phi_1^{'}b_{23}\phi_3^{'} \\
 & & \phi_1^{'}b_{33}\phi_1^{'} & \phi_1^{'}b_{31}\phi_2^{'} & \phi_1^{'}b_{32}\phi_2^{'} & \phi_1^{'}b_{33}\phi_2^{'} & \phi_1^{'}b_{31}\phi_3^{'} & \phi_1^{'}b_{32}\phi_3^{'} & \phi_1^{'}b_{33}\phi_3^{'} \\
 & & & \phi_2^{'}b_{11}\phi_2^{'} & \phi_2^{'}b_{12}\phi_2^{'} & \phi_2^{'}b_{13}\phi_2^{'} & \phi_2^{'}b_{11}\phi_3^{'} & \phi_2^{'}b_{12}\phi_3^{'} & \phi_2^{'}b_{13}\phi_3^{'} \\
 & & & & \phi_2^{'}b_{22}\phi_2^{'} & \phi_2^{'}b_{23}\phi_2^{'} & \phi_2^{'}b_{21}\phi_3^{'} & \phi_2^{'}b_{22}\phi_3^{'} & \phi_2^{'}b_{23}\phi_3^{'} \\
 & & & & & \phi_2^{'}b_{33}\phi_2^{'} & \phi_2^{'}b_{31}\phi_3^{'} & \phi_2^{'}b_{32}\phi_3^{'} & \phi_2^{'}b_{33}\phi_3^{'} \\
 & & & & & & \phi_3^{'}b_{11}\phi_3^{'} & \phi_3^{'}b_{12}\phi_3^{'} & \phi_3^{'}b_{13}\phi_3^{'} \\
 & & & & & & & \phi_3^{'}b_{22}\phi_3^{'} & \phi_3^{'}b_{23}\phi_3^{'} \\
 & & & & & & & & \phi_3^{'}b_{33}\phi_3^{'}
\end{bmatrix}.
$$

In the element level, the residual vector is expressed as follows:

$$
Q^e=\int_0^L \Phi^T\mathbf{f}ds-\int_0^L \hat{T}\Phi^{'T}\mathbf{r}^{'}ds\,. \tag{44}
$$

The second term in Eq. (44) can be further expressed as follows

$$
\mathbf{f}_e=-\int_0^L \hat{T}\Phi^{'T}\mathbf{r}^{'}ds=\begin{bmatrix}\hat{T}_0\mathbf{r_0}^{'}\\ \hat{T}_1\mathbf{r}_1^{'}-\hat{T}_0\mathbf{r_0}^{'}\\ -\hat{T}_1\mathbf{r}_1^{'}\end{bmatrix}, \tag{45}
$$

where $\hat{T}_0$ and $\mathbf{r}_0^{'}$ are determined in domain $s\in[0,L/2]$, and $\hat{T}_1$ and $\mathbf{r}_1^{'}$ are determined in domain $s\in[L/2,L]$.

4.1.3 Extended formula for multi-thread systems

To form the initial configuration of a web, multiple threads are placed in the Cartesian coordinate system (O-XYZ in Fig. 5-a) in which the connected nodes among threads share the same coordinate. At the initial state, the configuration of the web is estimated and a search for the equilibrium is followed.

In the fabric web, each thread is discretized in its own arc-length coordinate, s. The incremental equation for each thread can be obtained using the same formulations as Eq. (28) or (34). The incremental equations for individual threads are then assembled together to form the global stiffness matrix, **K**, and the global residual vector, **F**, for the web system. The assembly procedure is same as the stiffness and force vector assembly procedure in any commercial FEM

code. With the assembled finite element equation for the whole web, the incremental displacement, **U**, can be obtained to update the configuration of the web. By this means, the static equilibrium of the web system under any external load can be achieved. The solution procedure for the vibration problem is similar to the static problem and is not repeated here.

4.1.4 Examples

An analysis code has been then developed to simulate the large nonlinear deformation and high-fidelity stress distribution for the fabric system with arbitrary fiber configurations and under static and dynamic loads. This code is being extended to deal with more general textile fabrics with non-linear geometry effects and to be embedded in the meso-structural model for the textile composites.

Figure 6 demonstrates the new capability developed with solving a static equilibrium problem of a three-dimensional spider net-like fiber net. Figure 6-a illustrates the geometry of the spider net, while Fig. 6-b shows the resultant static deformation predicted using the formulation developed. Note that carbon fiber braided spider net may be used as the reinforcement in composite structures. The analysis code has been developed to simulate the deformation and stress for any carbon fiber net under given static and dynamic loads.

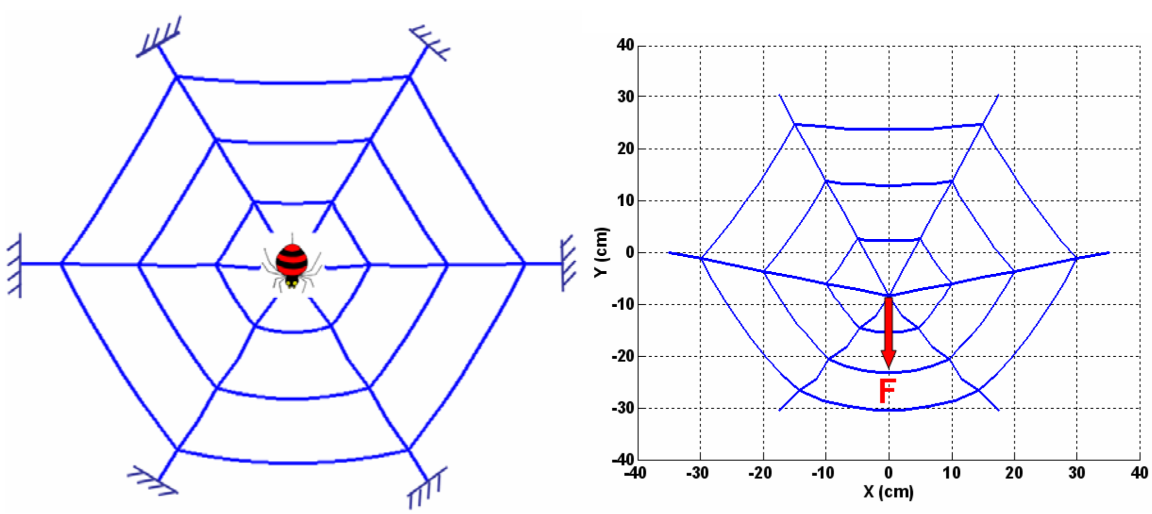

(a) A three-dimensional spider net (b) Deformation of the spider net under force F

Figure 6. The shape of a spider net and the corresponding deformation.

Figure 7 shows another example that an out-of-plane vertical load, F = 50,884 N, is applied to the spider net in the negative *z*-direction. The deformed net and the tension force in the net are

illustrated in Fig. 7-a and 7-b, which shows a maximum tension, 37,225 N, in the net under the given maximum impact load. The red color in Fig. 7-b indicates the maximum tension, while the other colors indicate other tension levels as shown in the color map.

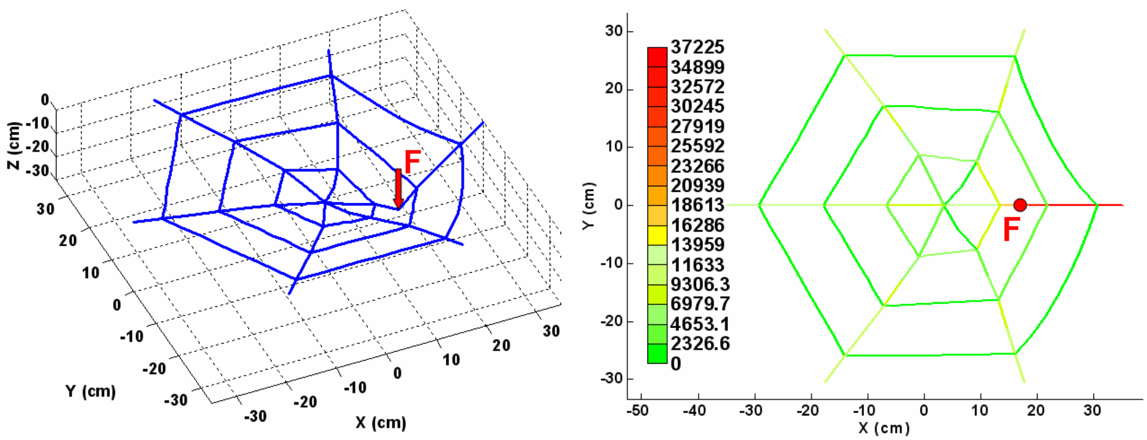

(a) Deformation shape (b) Tension distribution

Figure 7. A concentrated force, F=50,884 N, is applied at the red point in negative *z*-direction. a) Spider net deformation under the force F. b) The maximum tension force in the net is shown in red color with an amount of 37,225 N.

Figures 8 and 9 illustrate an example for demonstrating the new fiber modeling capability developed to simulate a tennis racket during tennis ball-racket interaction. The objective of the simulation example is to find out how a pretension can be determined for certain design purposes related to racket performance with a given tennis racket configuration. In this example, a tennis racket shown in Fig. 8 is considered, which has 16×19 strings with a diameter of 1.24 mm. The tensile modulus of the string is E = 90 GPa with a recommended pretension between 55 N and 62 N. Numerical tests have been done for various pretensions and forced out-plane displacements due to tennis ball-racket interactions. Figure 9-a shows an example result for predicted tension distribution in the racket strings under a given pretension and forced displacement, while Fig. 9-b illustrates the out-plane stiffness-displacement relationships under different pretensions. This is seen that out-plane stiffness of the tennis racket is non-linear with respect to the out-plane displacement and will increase nonlinearly with the pretension. This kind of results, with other available results from the simulation, for example, failure of the strings, could be very useful for designing an advance tennis racket. More discussions regarding how to use the new capability for real tennis racket design problem is however omitted in this report.

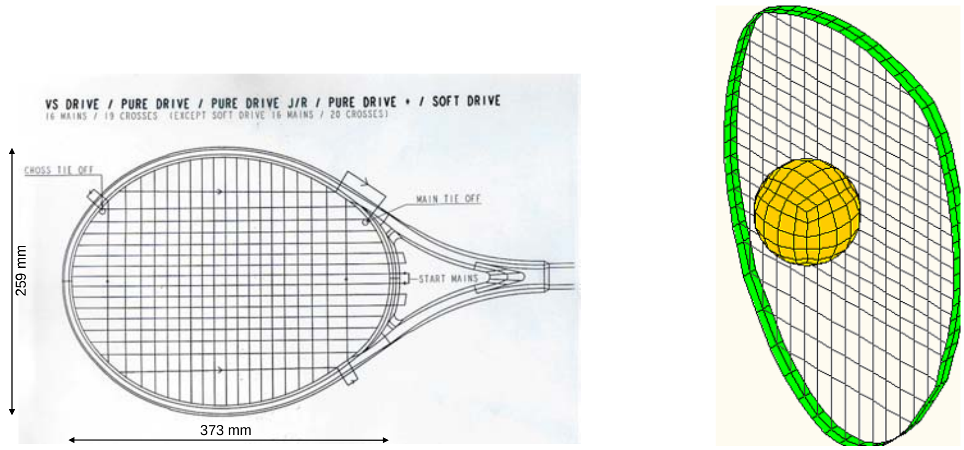

Figure 8. A tennis racket simulation problem

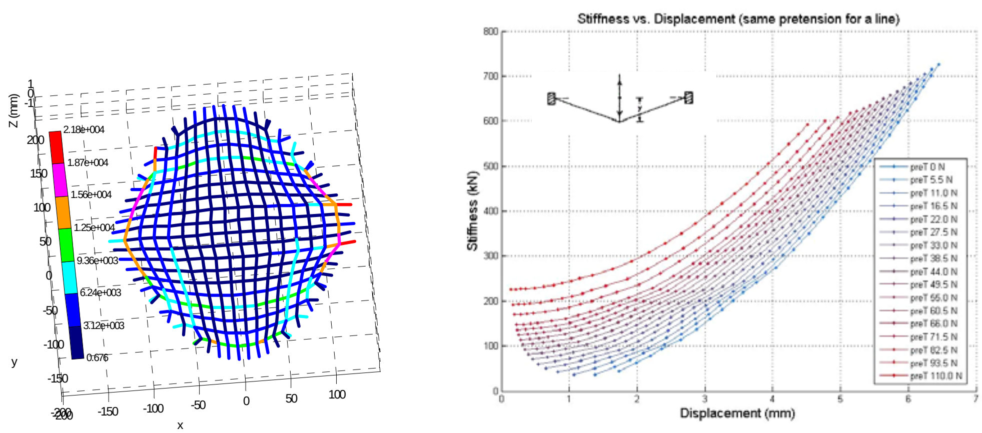

a) Example tension distribution

b) Predicted racket out-plane stiffness vs. maximum displacement and pretension

Figure 9. Example results using the new fiber model

The above examples have demonstrated the effectiveness of the new fiber model and associated simulation capabilities developed for designing a fiber or cable net system with high fidelity under arbitrary large deformation.

4.2 High Fidelity Meso-Structural Modeling of Textile Composite

In this task, we will develop a high-fidelity meso-structural model for general textile composite, which will include fiber/fabrics and filling/matrix material. This meso-structural model will allow us to conduct a detailed localized analysis for the meso-behaviors of the composite, which include nonlinear deformation and strength of individual fibers in the composite.

4.2.1 Modeling of fiber-fiber interaction

In the previous cable net models (e.g., in Fig. 6), it is assumed the cross threads share the same node at the crossing point, which implies: 1) cables are tied together with a knot and relative movement (e.g., slip) of crossing threads is not allowed at the knot, 2) effect of thread thickness (diameter) is ignored, and 3) most importantly, contact force between the threads can not be accurately predicted. In the current research, the nonlinear fiber model has been extended to consider thread to thread contact and effect of cross-section geometry of the threads. Figure 10 illustrates the new fiber-fiber interaction model (Fig. 10-b) with a comparison with the previous cable net model (Fig. 10-a) at the node.

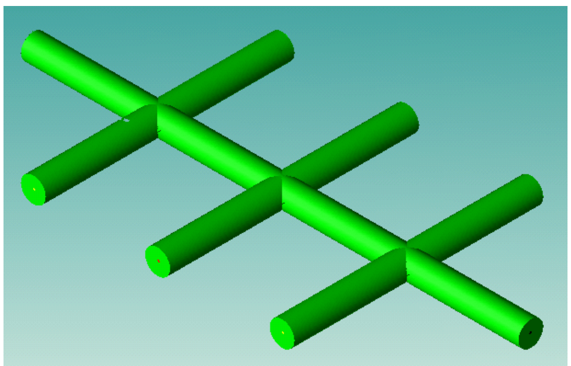

a) Previous cable net model

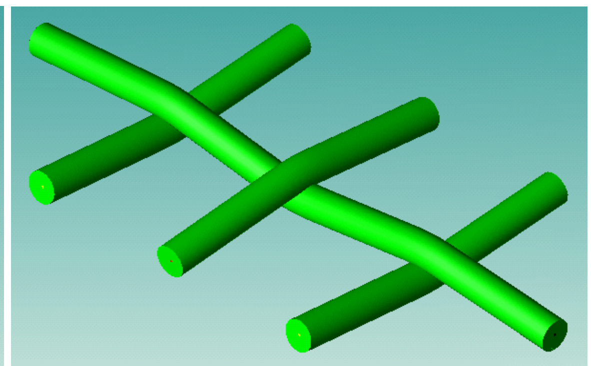

b) New fiber-fiber interaction model

Figure 10. Previous and new fiber-fiber interactions models

First, each thread is considered deformable along the radius direction with a diameter and stiffness coefficient. The action-reaction force between the threads is then determined by the relative deformation of the contacting treads. The deformation of each thread is also a function of the contact force. An iterative process has therefore been developed to obtain the converged results for both the contact forces and threads deformations.

Figure 11 and Table 4 compare the simulation results obtained with the two different fiber-fiber interaction models described in Fig. 10. Figure 11 illustrates the deformations (amplified by three times) and tension distributions in the woven fabrics, while Table 4 shows the out-plane stiffness and maximum and minimum tension values. Exactly the same boundary conditions were used in the two simulations, which fix the two ends of each fiber. A concentrated force, *F*=500lbs, is applied at the center of each woven fabric. As shown in Fig. 11 and Table 4, while higher tension is predicted with the new fabric model, the new model tends to distribute the

tension force more evenly in the fibers. As shown in Table 4, the new fabric model also results in a higher out-plane stiffness under the given force. Figure 11-a also shows that the maximum tension in the middle weft if the previous fabric model is used, while Fig. 11-b shows that the middle weft will have lower tension compared with the other two wefts. Physical explanation for this is that the tension in the middle weft has been partially relieved due to the applied force on the middle weft. This phenomenon can not be predicted with the previous fabric model. Therefore, the new fiber-fiber contact model is more accurate then the previous model.

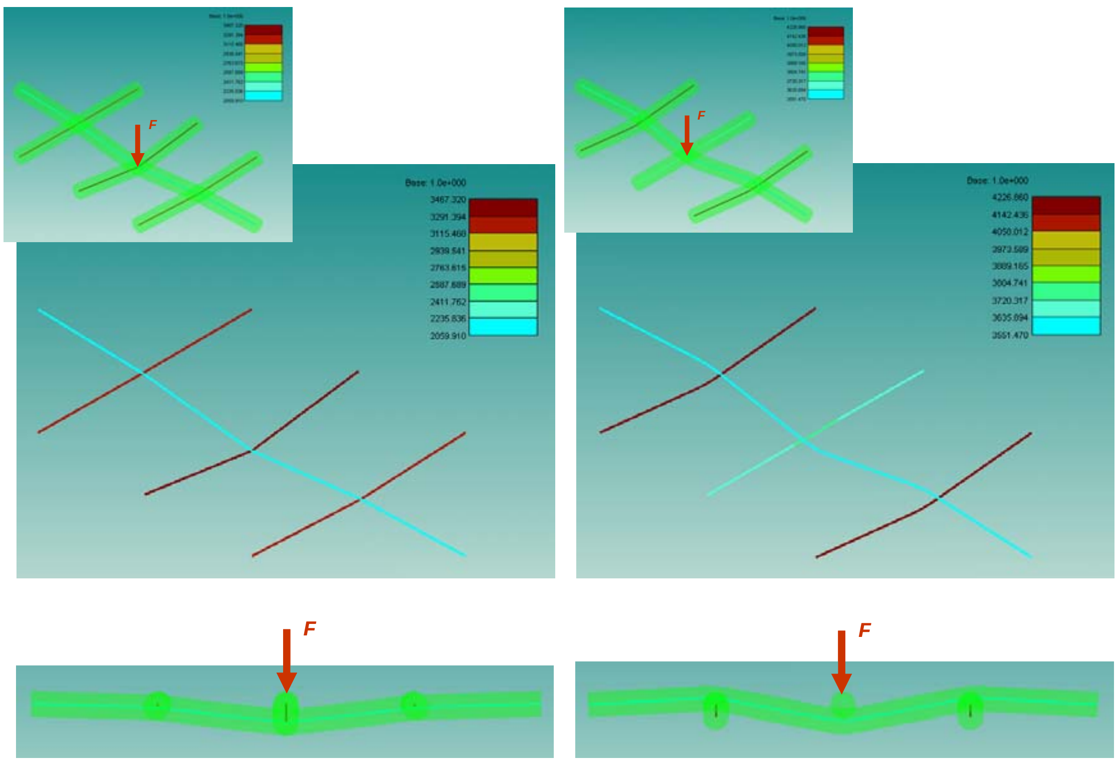

a) Previous cable net model b) New fiber-fiber interaction model

Figure 11. Comparison of previous and new fiber-fiber interaction models

Table 4. Comparison of predicted out-plane stiffness and tension

	Out-plane Stiffness	Maximum Tension	Minimum Tension	Tension Difference
Previous Model	1,020 lb/ in	3,470 lb	2,060 lb	1,410 lb
New Model	1,429 lb/in	4,230 lb	3,550 lb	680 lb

Figure 12 illustrates that the new fiber-fiber contact model can be further extended to deal with real woven and braided fabrics design problems with the design variables, such as: yarn width (Fig. 12-b and c), woven angle (Fig. 12-d), relative size (Fig. 12-e), and woven forces (Fig. 12-f). The preliminary results obtained in this report have demonstrated that the capability developed can be extended to evaluate widely different designs of woven composites for the purpose of improving structural performance and reducing weight. By applying an optimization process as discussed in Section 2.1.1, the technique can be further extended to find the optimum arrangement of the woven fibers in the composite for improved performance subject to the given weight, loading conditions, manufacturing cost, and other constraints.

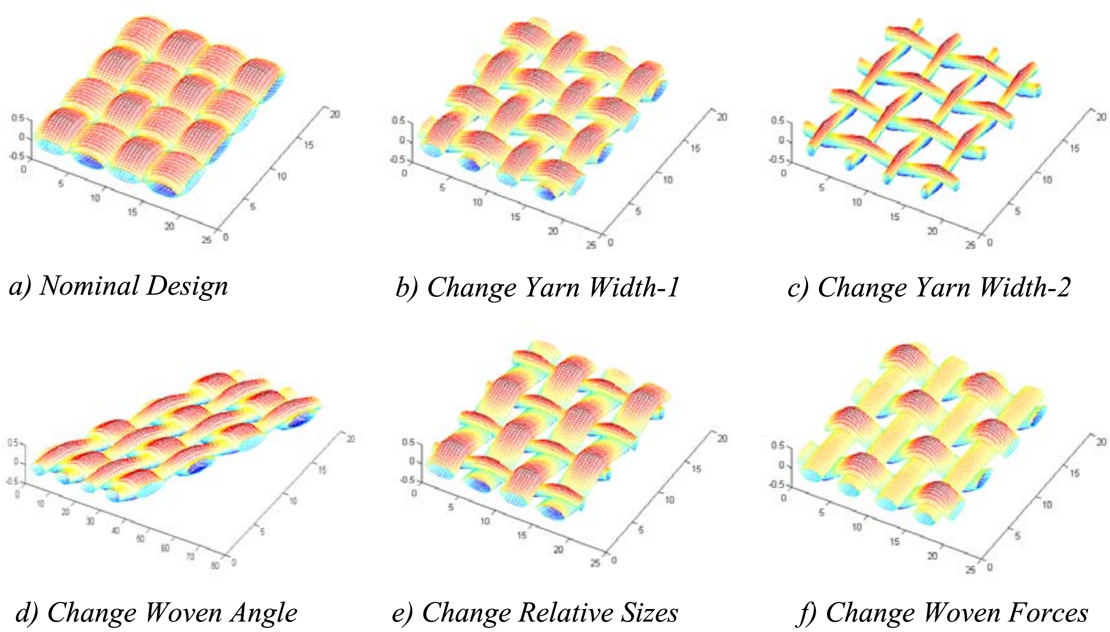

Figure 12. Example designs of a woven composite material (refer to [16]).

4.2.2 Development of an innovative composite concept

We are utilizing the new Function-Oriented Material Design (FOMD) methodologies to explore innovative structural and material designs. One example new concept material developed is termed *Biomimetic Tendon-Reinforced* (BTR) composite material. Figure 13 describes a design process, which demonstrates the feasibility of FOMD to lay out innovative concepts of composite materials. The example problem is to design a multi-layer composite material that features

functional outer and inner covers and a typical thickness as shown in Fig. 13-a. The middle layer between the outer and inner covers is considered to be a composite of two different materials: one is relatively stiff and forms the core structure (e.g., fiber reinforcements) for the major reinforcement; the other material is soft and acts as the matrix for the composite (which could be, for example, a polymer). Both materials are considered as functional materials. For instance, the fiber material may carry the major loads applied to the structure, while the matrix material could be an insulative material for the purpose of thermal, vibration, and/or acoustic managements. The objective considered in this example problem is to maximize the out-of-plane stiffness and strength due to an out-of-plane load by minimizing the total strain energy stored in the structure. The constraint function is the total amount of material used to build the structure between the outer and inner covers. The design problem is defined as shown in Fig. 13-a, and the optimal design for the design problem is obtained using the FOMD process, which is shown in Fig. 13-b. Figure 14 illustrates that the two-dimensional design in Fig. 13-b can be extended to a three-dimensional configuration.

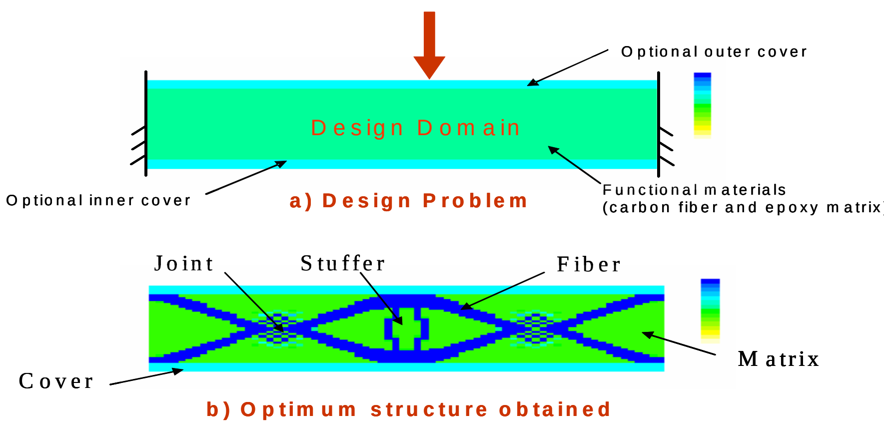

Figure 13. Design problem for back plate.

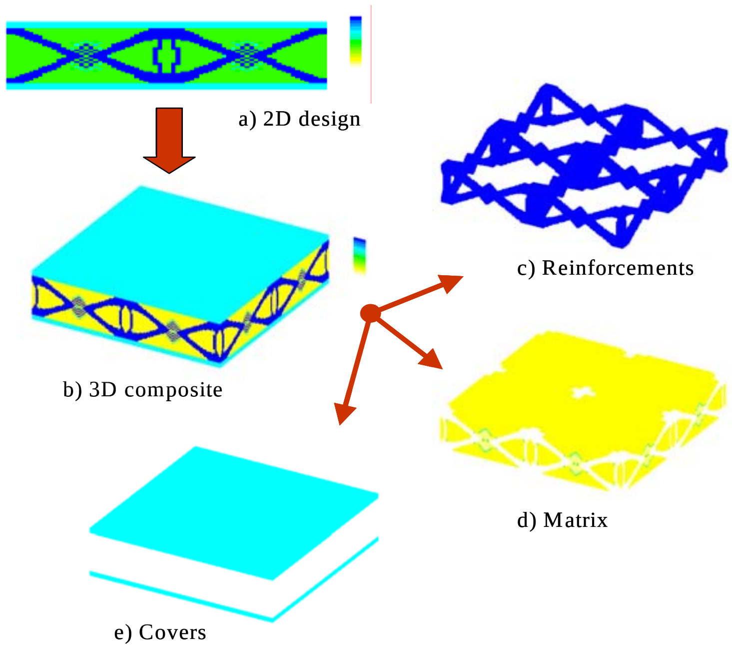

Figure 14. From two-dimensional design to a three-dimensional configuration.

The new concept material is termed *Biomimetic Tendon-Reinforced* (BTR) composite material. As shown in Fig. 15, the BTR composite includes five fundamental components: tendons/muscles (represented by fiber cables and/or tendon actuators), ribs/bones (represented by metallic or ceramic stuffers and struts), joints (including knots), flesh (represented by filling polymers, foams, etc.), and skins (represented by woven composite layers or other thin covering materials). Various BTR material concepts have been developed at U of M in collaborating with MKP Inc. for potentially different applications.

Biomimetic Tendon-Reinforced (BTR) Material
(© MKP Patent Pending)

Five fundamental components:

- **Tendons/muscles** – fiber cables and/or actuators
- **Ribs/bones** – metallic or ceramic stuffers and struts
- **Joints** – mechanical joints, fasteners, knots, etc.
- **Skins** – woven composite layers or other covering materials
- **Flesh** – filling polymers, foams, etc.

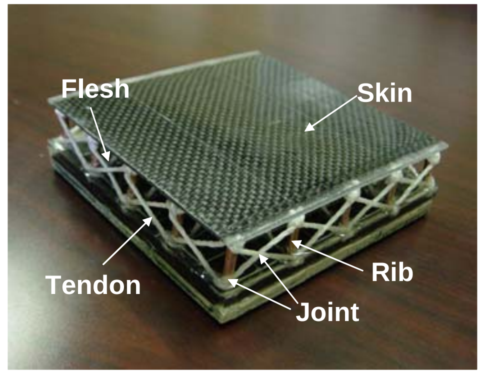

Figure 15. BTR composite material concept developed at MKP Inc.

Figure 16 illustrates two example BTR concepts and associated fabrication processes. Figure 16-a shows a BTR material with bead stuffers, carbon fiber/epoxy skin, and Kevlar tendons, while Fig. 16-b shows one with rod stuffers, Kevlar fiber/epoxy skin, and Kevlar tendons. These materials are ultra-lightweight and can be fabricated using the weaving processes shown in Figs. 16-a and b. The BTR concept will result in a new and innovative kind of composite materials: unlike traditional woven materials, in which the fibers are nearly evenly distributed in one plane in the matrix material, the new material will be reinforced by allocating concentrated fibers, such as fiber ropes, along load paths so as to increase transverse stiffness. MKP has filed a patent for this new BTR material concept.

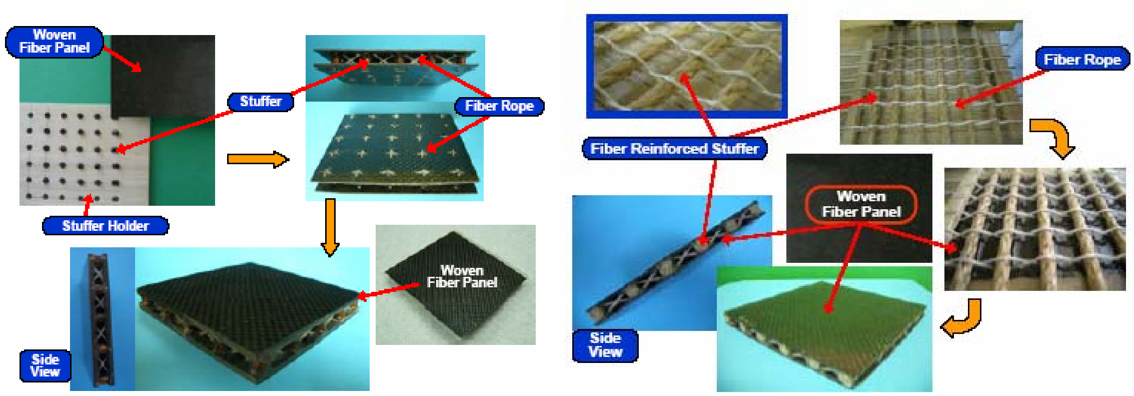

a) BTR with bead stuffer b) BTR with rod stuffer

Figure 16. Example BTR materials and fabrication processes developed at MKP Inc.

We are exploring the use of the above composite material concept for various applications. Several example BTR prototypes have been developed at MKP, as shown in Fig. 17. Figure 17 illustrates three BTR prototypes (Fig. 17 b-d) previously developed at MKP. We will select one configuration of the concept designs, through virtual prototyping and experiments, for a back plate in a composite armor. We will further design and fabricate a mold with the fixtures for fabricating the back plate in a cost-effective and efficient way. With the new mold, a number of sample back plates will be made, which will be used for basic mechanical tests and possible ballistic tests.

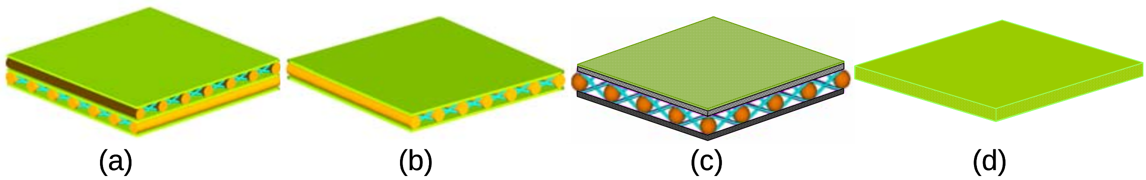

Figure 17. Options for composite plate design: a) Composite plate with multi-layered rod stuffers; b) Composite plate with rod stuffers; c) Composite plate with bead stuffers: d) Conventional laminate composite

The potential benefits of using the BTR composite have been investigated. A two-dimensional concept BTR composite is shown in Fig. 18-a, which is composed of glass fiber tendons and alumina stuffers. For comparison, a conventional S2 glass laminate is also modeled with the same size, which is shown in Fig. 18-b. The elastic property and strength of the S2 fiber/epoxy material and alumina material are listed in Table 5.

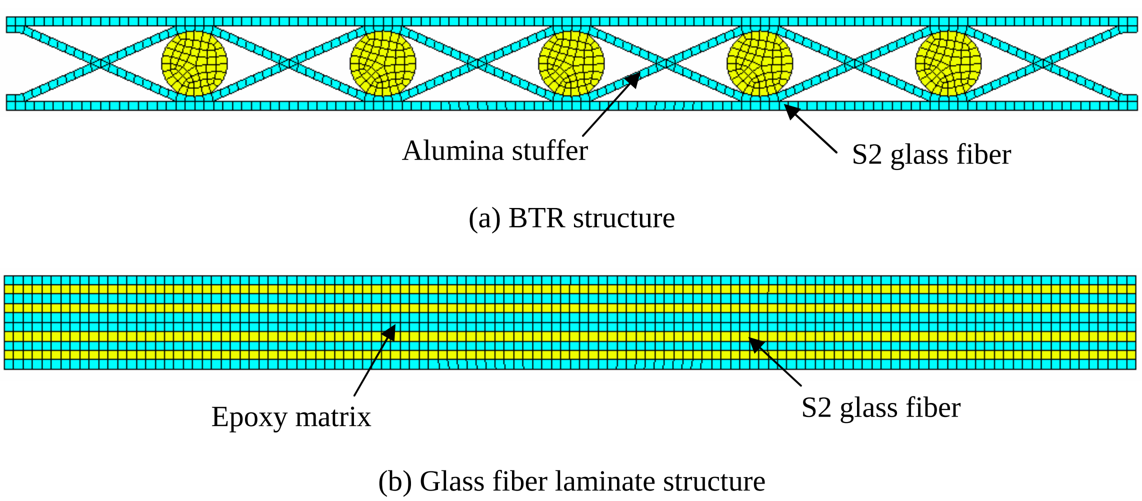

Figure 18. Finite element models for BTR and traditional laminate composites.

Table 5. Material properties used for composite analysis

Glass fiber with epoxy	Elastic Properties				
	E_a (GPa)	E_t (GPa)	ν_a	ν_t	G_a (GPa)
S2/3501-6	55.9	18	0.27	0.27	7.6

Glass fiber with epoxy	Composite Strength					
	S_1^t (GPa)	S_1^c (GPa)	S_2^t (GPa)	S_2^c (GPa)	S_{12} (GPa)	S_{23} (GPa)
S2/3501-6	1.79	0.96	0.06	0.16	0.11	0.083

Glass fiber with epoxy	Fracture Properties	Density
	G_{1c} (J/m^2)	ρ (g/cc)
S2/3501-6	160	1.99

stuffer	Elastic Properties		Compressive Strength	Density
	E (GPa)	ν	S^c (GPa)	ρ (g/cc)
Alumina (99%)	370	0.22	3.0	3.96

(E_a is fiber axial modulus, E_t is fiber transverse modulus, ν_a is axial Poisson's ratio, ν_t is transverse Poisson's ratio, and G_a is axial shear modulus. S_1^t is fiber axial tensile strength, S_1^c is fiber/epoxy axial compression strength, S_2^t is fiber/epoxy transverse tensile strength, S_2^c is fiber/epoxy transverse compression strength, S_{12} is fiber/epoxy in-plane shear strength, and S_{23} is fiber/epoxy out-of-plane shear strength.)

In the current simulation, a blast load is represented as an overpressure on the composite. The two-dimensional composite panel in Fig. 19 has a dimension 36 cm – 3 cm in length and thickness. The panel is clamped at both edges along the length. A peak overpressure, 112 MPa, is reached at the top center of the panel with an 8-kg TNT explosive charged 50 cm above the top center of the panel. The pressure was assumed to decay exponentially following the peak load. The structural responses of the composite panels with the peak overpressure are analyzed and shown in Fig. 19.

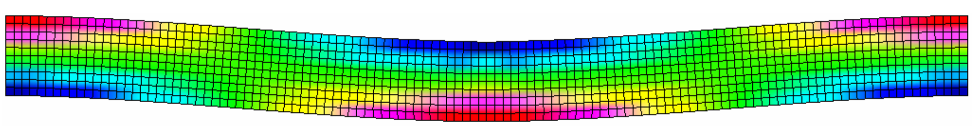

(a) Laminate composite

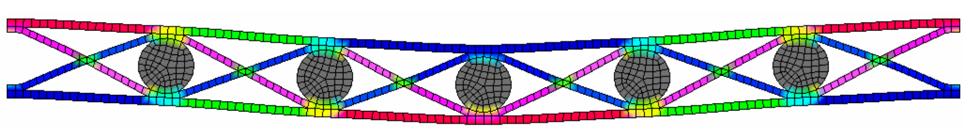

(b) BTR composite

Figure 19. Comparison of BTR composite with traditional laminate composite under a blast load (tensile stress in fibers.)

The appropriate failure modes of the two composites are summarized in Table 6. The weight and mechanical properties of the BTR composite panel and laminate composite panel are compared in Table 7. It is seen that the BTR composite has superior strength (approximately 2.5 times) compared to the conventional laminate panel under the blast loading. The BTR panel is also much lighter than the laminate panel. However, the out-of-plane rigidity of the BTR panel is reduced to 55% of the laminate composite panel.

Table 6. Failure modes for BTR and laminate composite panels under blast

Failure mode	*BTR composite*	*Laminate composite*
Fiber failure	Tensile stress in fibers	Tensile/compressive stress in fibers
Matrix/stuffer failure	Stuffer compressive stress	Transverse normal stresses and shear stresses
Delamination	Not applicable	Through the thickness normal stress and applicable shear stresses

Table 7. The comparison of BTR composite and laminate composite

	Weight (normalized)	Out-of-plane rigidity (normalized)	Strength* (normalized)
BTR	68 %	55 %	245 %
Laminate	100 %	100 %	100 %

(* The BTR strength index is calculated as the maximum fiber tensile stress divided by fiber axial tensile strength; the laminate strength index is calculated using the equation in Yen and Jones [17].)

4.2.3 Modeling of fiber interactions with other materials in a composite

The true nonlinear fiber model has been extended to consider interaction with other materials, for example, stuffers and matrix, in a composite. The resultant capability has been utilized to simulate response of a BTR composite under a blast loading. Figure 20-a shows the predicted displacement and tensile stress in the BTR structure under the same blast loading as applied in Fig. 20-b, while Fig. 20-b shows the results obtained using a conventional finite element model. The predicted maximum tensile stress in the fiber tendon is 385 MPa using the true nonlinear model, which is larger than the maximum axial tensile stress (307 MPa) obtained from the conventional FE model. Since the non-compressibility of the fiber tendon is considered in the current model, the result in Fig. 20-a is supposed to be more accurate than the FEA result. The tensile stress distribution obtained from the true nonlinear cable model is also much smoother than the result from conventional FE model, which indicates that the nonlinear cable model can capture the instant stress wave propagation in the cable network under blast. The true nonlinear cable model will be further extended and correlate with the experimental results and then

implemented into optimal design system for designing advanced BTR structure with much improved performance.

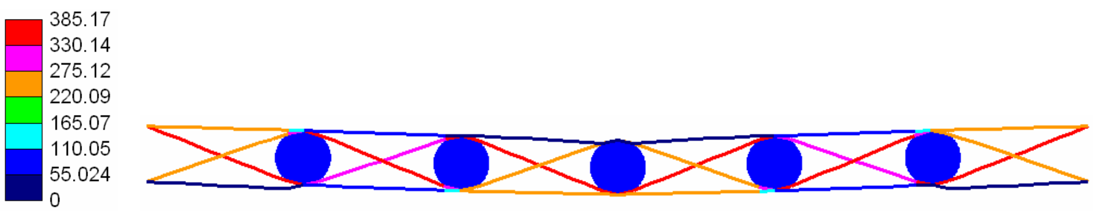

(a) Result obtained using the true nonlinear cable model

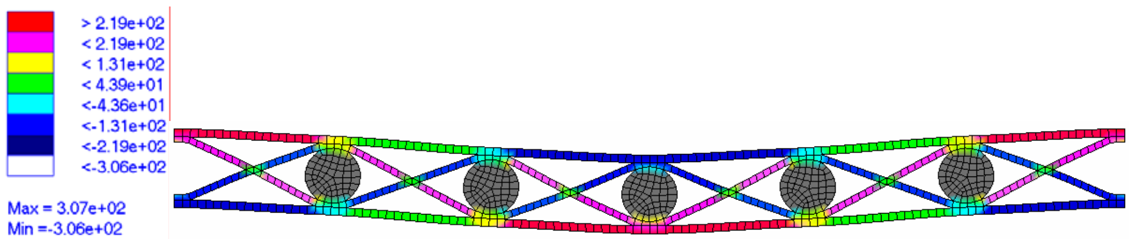

(b) Result obtained using the conventional finite element model

Figure 20. Comparison of tensile stress (MPa) in fiber tendons under blast loading using different simulation models.

The BTR composite concept features ultra-light weight and outstanding out-of-plane stiffness/strength, which can also provide superior protection against shock wave in a blast event. Note that according to our knowledge, back plate will have significant effect on armor performance. Our back plate with BTR composite concept will be designed to have maximum bending stiffness and strength with a minimum weight for given armor applications. The preliminary results shown in this report can be further extended to deal with other problems such as compression strength, buckling stability, and impact resistance, which will be major tasks in next phase of this research program. Moreover, multiple objective functions can be considered for designing a composite structure with multiple roles in an advanced vehicle system.

The non-linear fiber model is being further extended to consider fiber-matrix interaction in a general composite material. Figure 21 illustrates such geometry model has been developed with a focus on predicting meso-behavior of a composite and its delamination and de-bonding phenomena as well as associated damage mechanism.

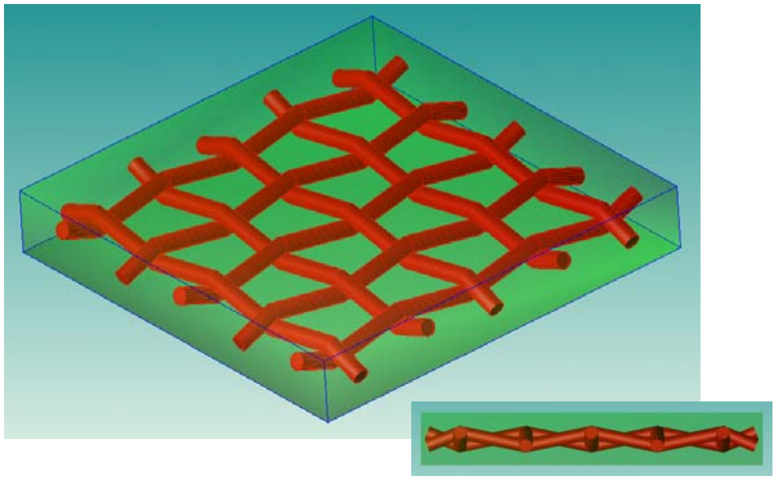

Figure 21. An example model of fiber-matrix interaction.

In summary, we have extended our nonlinear fiber model to general three-dimensional fabric system with various configurations for simulating practical textile fabrics and composite materials. The formulation will account for geometry nonlinearity and arbitrary large deformation of the textile fabrics. This results in a unique capability for simulating textile composite materials, especially for the damage assessment. The new capability will be further extended and integrated with the other advanced capabilities being developed for designing truly optimum composite for various applications.

4.2.4 Example results

4.2.4.1 Simulating a simple multi-fiber interaction model

Figure 22 illustrates a simple model for a fiber-fiber contact problem with two crossing-over threads. As shown in Fig. 22, each thread is fixed at the both ends with a given pretension, which is defined by an initial tensile strain, e_i (where $i = 1, 2$). The thread-to-thread interaction results in a contact force between the two threads, which is a function of pre-selected design parameters, such as thread diameter *D* (for the both threads) and pre-tensions (defined by initial tensile strains e_1 and e_2 in Fig. 22). Three examples have been simulated with: 1) *D*=2.0, e_1=e_2=0.94%, 2) *D*=2.0, e_1 =0.94%, e_2 =2.0%, and 3) *D*=1.2, e_1 =e_2 =0.94%. The same tensile modulus, *EA*=2.5e5, is used for all the three examples.

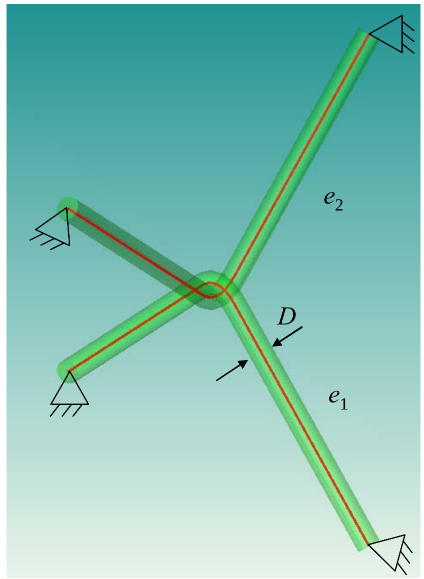

Figure 22. Simulation model of a simple fiber-fiber contact problem

Figure 23 shows the results obtained using the new fiber-fiber contact model for the three examples. It is seen that increasing the initial strain in thread #2 by 113% results in a 23% increase of the contact force (comparing Fig. 23-b with Fig. 23-a), while reducing thread diameter by 40% will reduce the contact force by 81%. With this kind analyses enabled by the new capability developed, we can design a fabric system with necessary detailed information for various design purposes, such as reducing potential fiber failures in a fabric system.

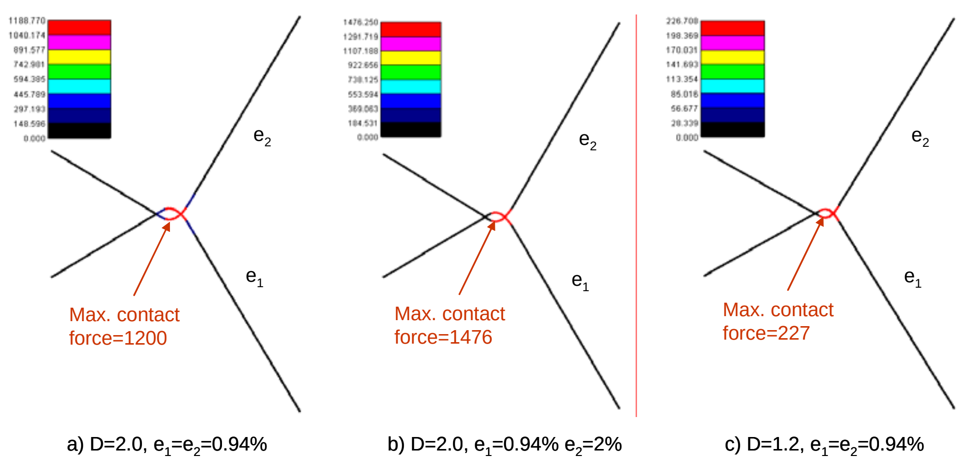

Figure 23. Example results for using different design parameters

4.2.4.2 Simulating a braided fabric

The second example is to demonstrate the new capability developed can be used to simulate a very general fabric system. A simulation model with a warp fiber and three weft fibers is shown in Fig. 24. As shown in Fig. 24, each fiber in the model is fixed at the both ends, and a 2.04% pre-tension strain is applied initially to all the fibers. Figure 25 and Table 5 illustrate example simulation results obtained using the simulation code for four different cases: a) nominal case, *EA*=2.5e5, *D*=2.0; b) doubled tensile modulus, namely, *EA*=5.0e5, *D*=2.0; c) reduced fiber diameter, *EA*=2.5e5, *D*=1.0; and d) only the warp tensile modulus is doubled, namely, *EA*=5.0e5 for the warp, *EA*=2.5e5 for wefts, and *D*=2.0. Figure 25 shows that tension distribution in the fabric system becomes very different under different design parameters. For example, reducing fiber diameters of the fibers results in tension to be more evenly distributed in the braided fibers (comparing Fig. 25-c with Fig. 25-a), while using different fibers for the ward and wefts (e. g., doubling the warp tensile modulus as shown in Fig. 25-d) results in more unevenly distributed tension in the fabric system. Table 5 further compares the actual tension values for the four cases, which include maximum and minimum tensions and difference between them. It is seen that doubling the tensile modulus for all the fibers will almost double the tension in the braided fibers, while doubling only the warp tensile modulus will results in a 23% increase in the maximum tension and 31% increase in the minimum tension. Again, these kind results can be used to design a braided fabric with desired material properties and damage tolerance.

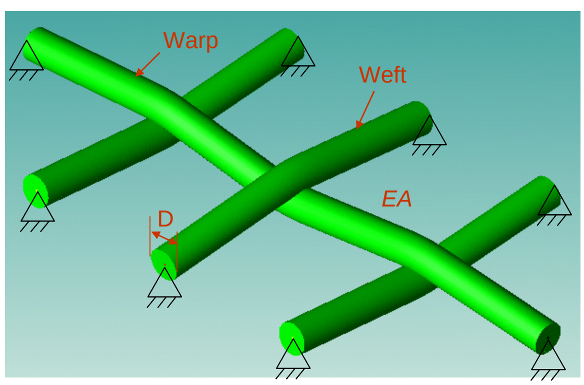

Figure 24. Deformation of braided fibers under a 2.04% pretension strain.

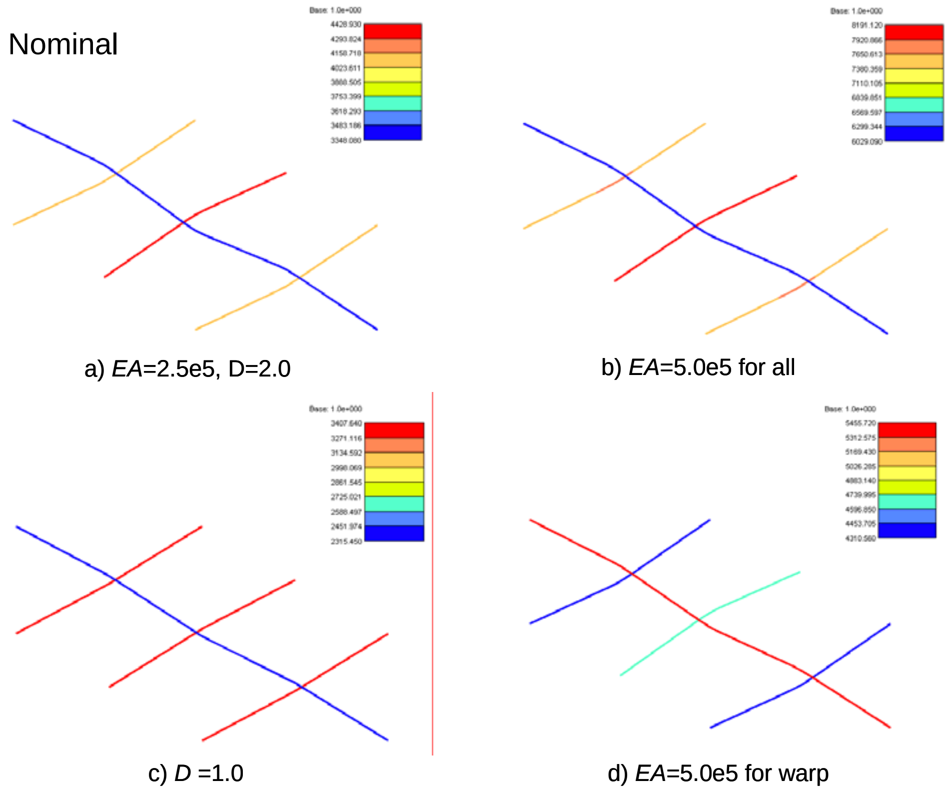

Figure 25. Comparison of predicted tensions for different parameters (*EA*: tensile modulus; *D*: diameter of the fibers).

Table 5. Comparison of tension values (N)

	Maximum Tension	Minimum Tension	Tension Difference
a) *EA*=2.5e5, *D*=2.0	4,429	3,348	1,081
b) *EA*=5.0e5, *D*=2.0	8,191	6,029	2,162
c) *EA*=2.5e5, *D*=1.0	3,408	2,315	1,093
d) *EA*=5.0e5 for warp, *D*=2.0	5,456	4,311	1,145

4.2.4.3 Simulation of a waiting material concept

Figure 26 illustrates an example composite structure, which is made of carbon fibers and aluminum stuffers. This structure represents a novel backplate composite concept for an advanced armor, which is also used to illustrate the concept of multi-stage stability of the concept

structure. The key idea of the sample composite structure is the embedded woven fiber ropes. When a load carrying thread is broken, the neighboring threads can act as the safety members to reserve the integrity of the whole structure provided the threads are properly placed. As shown in Fig. 26, five metallic beads are utilized as the stuffers in a braiding process to form a woven lattice composite. The integrity of the composite structure is supported by the pre-tensioned fabric ropes. When a rigid object is impacted on the composite, the deformation of the structure and the corresponding tension force in the rope can be obtained by using the nonlinear analysis model developed by us.

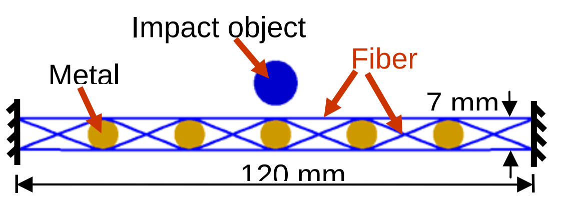

Figure 26. The sample composite structure for multi-stage stability illustration

Figure 27 illustrates the basic concept of the multi-stage stability in the composite structure. The maximum permissible tensile force in the threads is 3,800 N. In Fig. 27-a, the flying object hits the composite structure, the maximum deflection of the composite structure becomes 2.5 mm, while the magnitude of the tensions in the threads is shown in the colormap. It is seen that the tension in the master thread (shown in red) is close to the strength limit, and the neighboring thread (shown in green) is going to take effect in the next stability stage. In Fig. 27-b, the stability stage B reaches its limit, the red thread is going to break, while the cyan neighboring thread is going to act in stability stage C. Figure 27-c shows the stability stage C. It is seen that the central metal stuffer is separated from the fabric net, while the net is still stable with the automatic position adjust of the remaining four metal stuffers. In Fig. 27-d, the final stability stage is reached, and the maximum bending deflection of the composite structure is 16 mm.

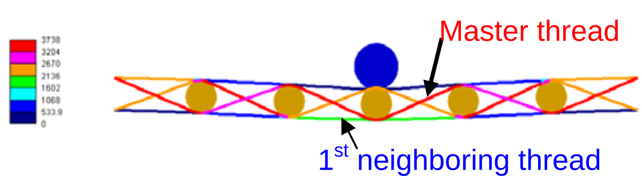

a) Stability stage A, all the fiber threads are intact; the maximum deflection is 2.5 mm.

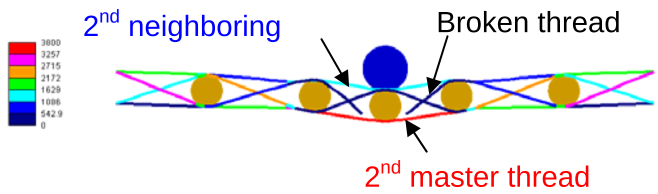

b) Stability stage B, the first master thread is broken, the first neighboring thread becomes the master thread, the maximum deflection is 4.3 mm.

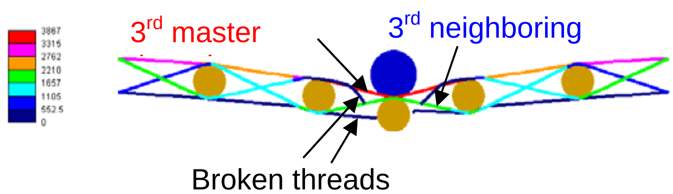

c) Stability stage C, the first and second master threads are broken, the second neighboring thread becomes the master thread, the maximum deflection is 8.3 mm.

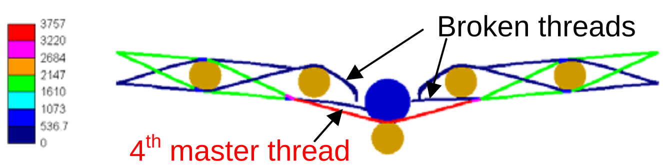

d) Stability stage D, all master threads are broken except the third neighboring thread now becomes the master thread; the maximum bending deflection is reached as 16.0 mm.

Figure 27. The multi-stage stability of the composite structure during impact.

The reaction force on the impact object is shown in Fig. 28. In the four stability stages, the reaction force in stage A and stage B are almost linear in terms of the deflection. In the last two stability stages, the composite structure can still provide sufficient bending stiffness. Figure 28 evidences the existence of multi-stage stability and the effectiveness of the fiber ropes in the composite structure.

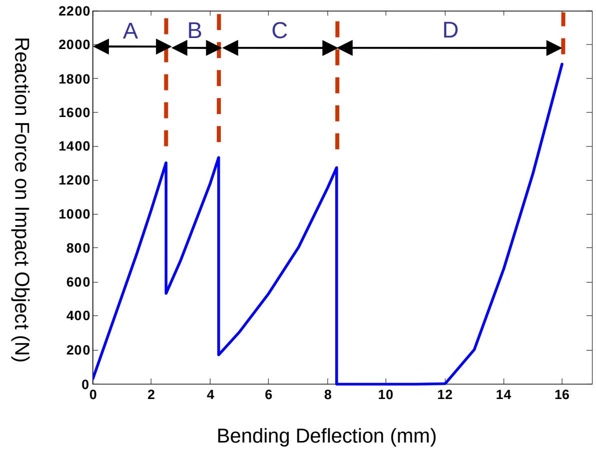

Figure 28. Reaction force on the impact object versus the bending deflection of the composite structure

4.2.5 Future development

Figure 29 illustrates a complete fiber-reinforced composite model to be developed in next step, which will be used to predict material behaviors at the meso-level. A general homogenization method will be then developed for predict effective material properties of composite for structural analysis and design at the macro-level. The developed new capabilities will be finally implemented into the FOMD system for optimal design of composite structures for a wide range of different applications.

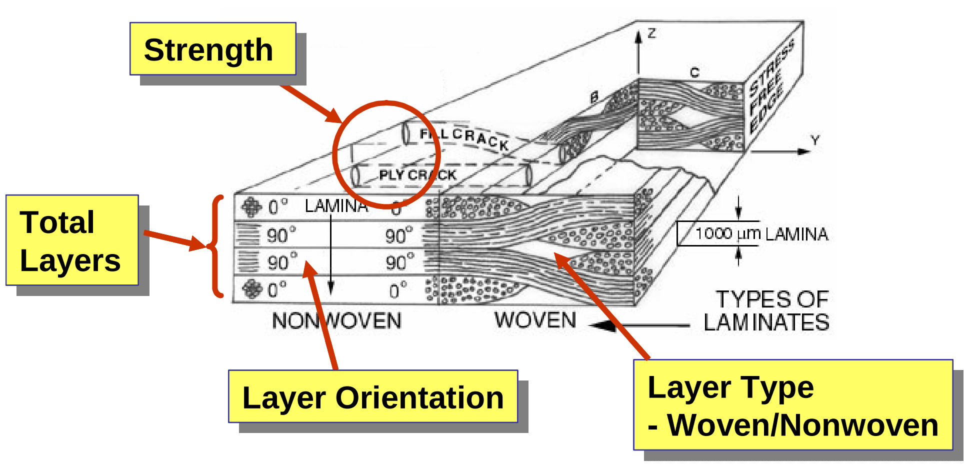

Figure 29. A completed design model for fiber-reinforced composites

4.3 Potential Applications

Figure 30 shows a snapshot of the damage and deformation simulation for a HMMWV under a mine attack. The landmine is detonated under the driver seat. As can be seen in Fig. 30, the floor under the seat has been significantly damaged. The resultant acceleration on the dummy can also been predicted. As in this case, the dummy will be seriously injured if no additional protection is provided.

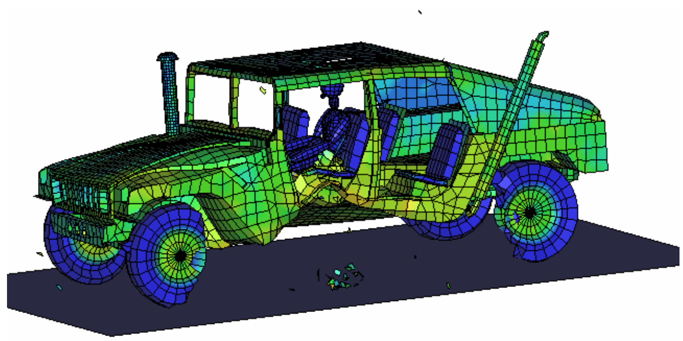

Figure 30. Example result of a landmine-HMMWV-dummy blast simulation.

Blast simulations have also been carried out for investigating blast effects on special substructures in the vehicle system. Figure 31-a demonstrates that special blast effect – the window glass blowout under the blast wave can be simulated using the simulation model. It is seen that once the blast wave arrives, the glass is broken to pieces and blown out from the window, which matches the actual test results. Figure 31-b further illustrates that the capability could be used to design a protective armor between the glass and driver for an existent vehicle system against the glass fragments in the blast event.

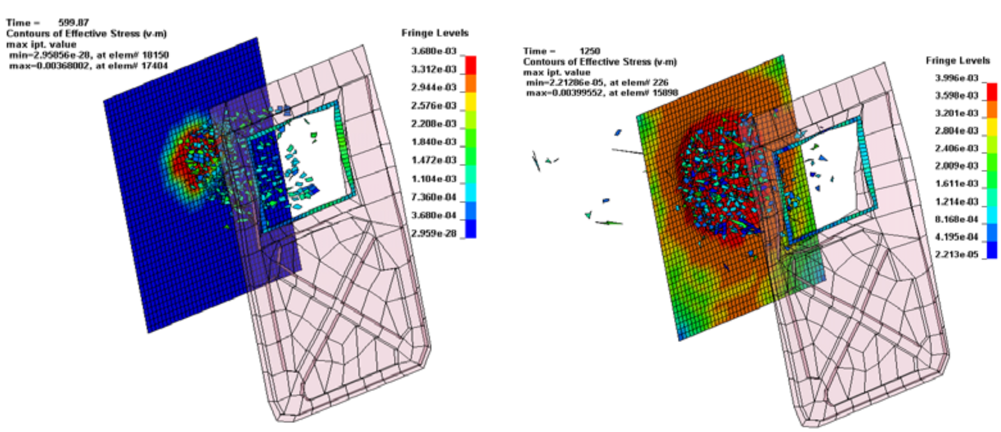

a) Glass blowout under the blast wave   b) Glass fragments penetrating an armor plate

Figure 31. Window glass blowout under a blast.

For mine blast protection, structural/material design can be roughly divided into two categories: 1) design of the protection panel (steel/composite) for blast wave deflection, and 2) material design for blast energy absorption.

In order to protect the crew members and the integrity of the main structure, protection panels are inserted in military vehicles to deflect the blast wave. Figure 32 illustrates an example design of the centerline "V-deflector" assembly, including "wing" deflectors that are added to ensure adequate deflection of the blast-wave away from the cab. Note that a Crew Protection Kit (CPK) prototype has been developed under DARPA support [21].

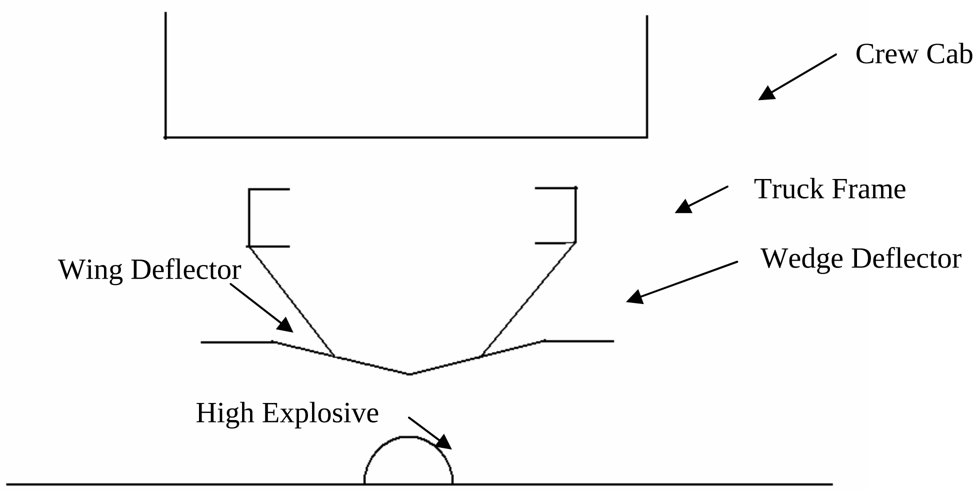

Figure 32. Example design of wing/wedge deflector geometry [22].

The successfully developed crew/vehicle protection kit can increase crew survivability of tactical wheeled vehicles subject to mine blast. However, these CPK's were based on a conventional steel/aluminum construction, and are close to a half ton in weight. In order to reduce the weight, sandwich structures have been proposed and tested as an alternative [23]. Experiments have been carried out for the composite panel under blast. It is found the panel cannot restrain the maximum deflection as much as the original alloy panel [23]. Due to the deficiency in inter-laminar strength of the sandwich panel's faces and the subsequent consequence from dynamic blast loading, the dynamic deflection of the panel is not satisfactory compared to the past monolithic panel test results. As studied by Yen and Jones [24], the failure of the composite panel has the following modes:

- Fiber failure in a blast loaded sandwich panel.

- Delamination induced by in-plane shock wave.
- Through-the-thickness compressive failure and spall fracture.

It is believed that the deficiency may be corrected with the following improvements:

- Orient some volumes of fibers or other types of solids in the through-the-thickness direction;
- Optimize ply layup, ply type, and matrix type to lower transverse tension.

Figure 33 illustrates the capabilities that have been developed by us in a FOMD-Blast system for predicting the pressure due to the blast wave on a composite plate. In addition to the blast wave, using the new (under developing) mine-soil-composite interaction model, the inhomogeneous property of soil, and the interactions between the blast wave and soil debris can be accounted for in the blast load prediction so that the composite structure can be optimized with more realistic loading conditions. A statistical algorithm will be developed for various soil behaviors under the land explosive, including soil texture, structure, failure properties, wet/dry condition, etc. The effects of burial depth and debris-blast wave interaction will also be studied to calibrate the dependence in blast energy capture of the structure.

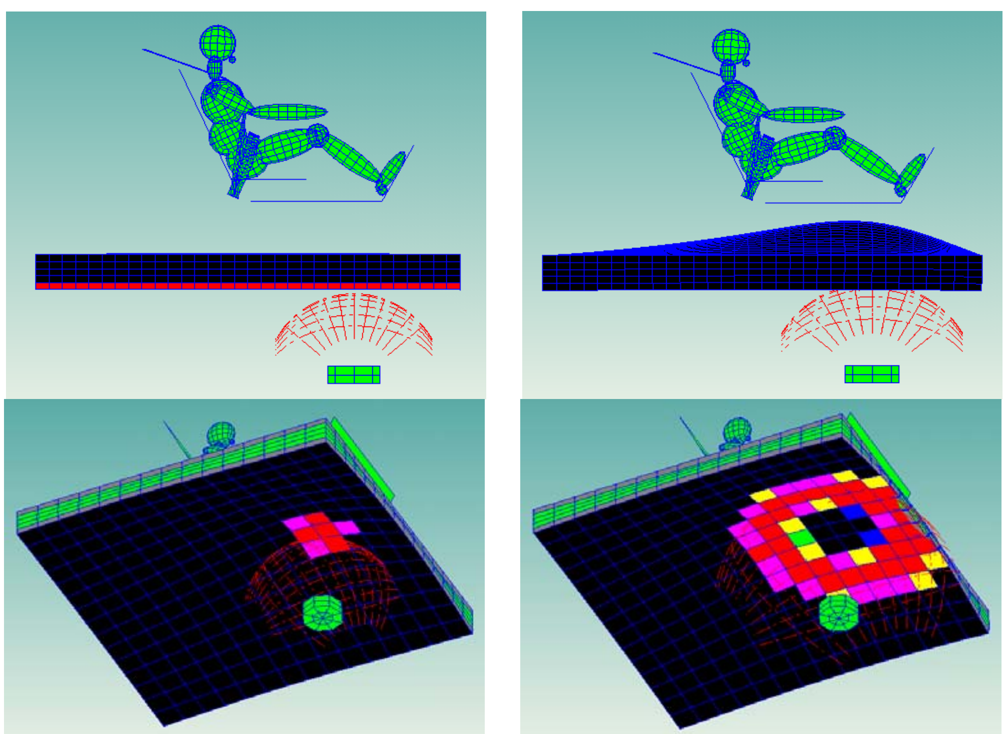

Figure 33. Blast wave pressure modeling in the FOMD-Blast.

Figure 34 illustrates the FOMD-Blast main menu for defining composite layout, which is used to select raw materials in the BTR-*Bl* composite and lay out the composition configuration. As shown in Figure 34, the BTR-*Bl* composite can be configured with a wide choice of different raw materials for the skin, core plate, stuffer, fiber, matrix, etc., and the designer can have great freedom to create an innovative configuration of the BTR-*Bl* composite with needed efficiency and convenience.

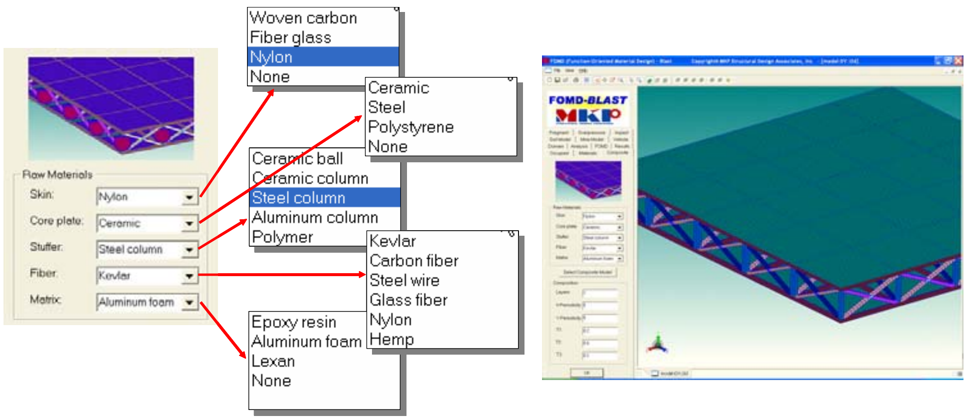

Figure 34. FOMD-Blast main menu for composite layout: selecting raw materials and configuration.

The present armor concept to defeat light to medium threats typically consists of a hard-strong frontal surface and a softer-tough and strong backing. In addition to ballistic and blast protections, other major requirements for advanced vehicle armor are lightweight, flexibility, maintainability and reduced life-cycle cost. Lightweight is crucial to maintaining excellent road and cross-country mobility, which is directly related to military deployability and survivability. Lightweight is also crucial to the transportability and sustainability as well as to structural integrity and durability. Flexibility means the armor structure can be shaped or formed to fit various vehicle contours. Maintainability implies two things: 1) the integrated armor system can be easily installed and removed from the vehicle with minimal time and manpower, and 2) the armor can be easily repaired during war time without replacing the whole armor structure. Life-cycle cost is directly related to affordability by the US military and the wide application of the armor system. The new integrated composite design capabilities can be used to design truly optimum and innovative composite structures for suiting the above needs.

5 CONCLUSIONS

Meso-structure of textile composites contributes to the outstanding properties of the composites, and at the same time becomes great challenge for simulation and design with needed accuracy and fidelity. We proposed to developed unique capabilities for modeling and simulation of textile fabrics and textile composites based on a truly nonlinear model developed by us. A damage model for textile composites will be then developed based on the meso-structural behaviors of the composite and the use of an enhanced homogenization method. The proposed research will contribute significantly to the related Army research areas for achieving the Army next ten years goals.

6 BIBLIOGRAPHY

[1] Ma, Z.-D., Wang, H., Kikuchi, N., Pierre, C., and Raju, B., Function-Oriented Material Design for Next-Generation Ground Vehicles; Symposium on Advanced Automotive Technologies, *2003 ASME International Mechanical Engineering Congress & Exposition*, November 15-21, Washington, DC, 2003, received the **Best Paper Award** from ASME Design Division. 2003.

[2] Ma, Z.-D., Kikuchi, N., Pierre, C., and Raju, B., "A Multi-Domain Topology Optimization Approach for Structural and Material Designs," ASME Journal for Applied Mechanics, Vol. 73, No. 4, pp. 565-573, 2006.

[3] Ma, Z.-D., Wang, H., Kikuchi, N., Pierre, C., and Raju, B., "Prototyping and Experimental Verification of Optimum Designs Obtained from the Topology Optimization," Structural and Multidisciplinary Optimization, in press. (2006)

[4] Ma, Z.-D., Wang, H., Kikuchi, N., Pierre, C., and Raju, B., "Substructure Design Using a Multi-Domain Multi-Step Topology Optimization," SAE Journal of Passenger Cars - Mechanical Systems, September 2004, pp. 1349-1358.

[5] Ma, Z.-D., Jiang, D., Kikuchi, N., Pierre, C., and Raju, B., "Multi-Domain Topology Optimization Using Advanced Substructuring Technique," 36th International SAMPE Technical Conference, San Diego, California, November 15-18, 2004.

[6] Wang, H., Ma, Z.-D., Kikuchi, N., Pierre, C., and Raju, B., "Joint Design for Advanced Ceramic Armor under Ballistic Impact," 36th International SAMPE Technical Conference, San Diego, California, November 15-18, 2004.

[7] Qi C., Ma, Z-D., Kikuchi, N., Pierre, C., Wang, H., and Raju, B., "Fundamental Studies on Crashworthiness Design with Multidisciplinary Objectives and Uncertainties in the System," 2005 SAE World Congress, received the Certificate of Appreciation from SAE.

[8] Ma, Z.-D., Wang, H., and Raju, B., "Function-Oriented Material Design of Joints for Advanced Armors under Ballistic Impact," 24th Army Science Conference, December 2004, Orlando, Florida.

[9] Wang, H., Ma, Z.-D., Kikuchi, N., Pierre, C., and Raju, B., "Multi-Domain Multi-Step Topology Optimization for Vehicle Structure Crashworthiness Design," 2004 SAE World Congress & Exhibition, Detroit, Michigan, March 8-11, 2004, SAE2004-01-1173.

[10] Ma, Z.-D., Wang, H., Kikuchi, N., Pierre, C., and Raju, B., “Substructure Design Using a Multi-Domain Multi-Step Topology Optimization,” 2003 SAE World Congress & Exhibition, Detroit, Michigan, March 3-6, 2003, SAE Paper 03B-125, pp.1-9, received the Certificate of Appreciation from SAE.

[11] Wang, H., Ma, Z.-D., Kikuchi, N., Pierre, C., and Raju, B., “Numerical and Experimental Verification of Optimum Design Obtained from Topology Optimization,” 2003 SAE World Congress & Exhibition, Detroit, Michigan, March 3-6, 2003, SAE Paper 03B-121, pp. 1-8.

[12] Ma, Z.-D., Kikuchi, N., Pierre, C., and Raju, B., “Multi-Domain Topology Optimization for Vehicle Substructure Design,” Symposium in Advanced Vehicle Technologies, Proceedings of 2002 ASME International Mechanical Engineering Congress & Exposition, November 17-22, 2002, New Orleans, Louisiana, IMECE2002-32908, pp. 1-10.

[13] Zheng-Dong Ma, Hui Wang, Yushun Cui, Douglas Rose, Adria Socks, and Donald Ostberg, , “Designing an Innovative Composite Armor System for Affordable Ballistic Protection,” 25th Army Science Conference, December 2006, Orlando, Florida.

[14] Zheng-Dong Ma, Dongying Jiang, Yuanyuan Liu, Basavaraju Raju, and Walter Bryzik, “Function-Oriented Material Design for Innovative Composite Structures against Land Explosives,” 25th Army Science Conference, December 2006, Orlando, Florida.

[15] Ma, Z.-D. and Jiang, D., Equilibrium and Vibration Analysis of a Fabric Web Under Abtrary Large Deformation, Proceedings of IDETC/CIE 2005, ASME 2005 International Design Engineering Technical Conferences and Computers and Information in Engineering Conference, September 24-28, 2005, Long Beach, California, USA, in press.

[16] Wang, H., Experimental Investigation and Hierarchical Modeling of FRP Materials for Automobile Application; *Ph.D. Thesis*, Dept. of Mechanical Eng., The University of Michigan, Ann Arbor, 2001.

[17] Hsiao, S.W., and Kikuchi, N., Numerical Analysis of Deep Drawing Process for Thermoplastic Composite Laminates, *Journal of Engineering Materials and Technology, ASME Transactions*, Vol. 119, pp. 314-318, July 1997.

[18] Terada, K. and Kikuchi, N., A Class of General Algorithms for Multi-scale Analyses of Heterogeneous Media, *Comput. Methods Appl. Mech. Engrg*, Vol. 190, pp. 5427-5464, 2001.

[19] Naik, N. K., and Ganesh, V. K., Prediction of On-axes Elastic Properties of Plain Weave Fabric Composites. Composites Science and Technology, Vol. 45, pp. 135-152, 1992.

[20] Ho, H., Tsai, M. Y., Morton, J., and Farley, G. L. In-plane shear testing of graphite-woven fabric composites. Experimental Mechanics, Vol. 45, pp. 45-52, 1994.

[21] Pytleski, J.L., and Catherino, H., Lightweight hull floor program, ARL-CR-58, U.S. Army Research Laboratory, Watertown, MA, 1993.

[22] Dillion, J., Strittmatter, K., Sergi, S., Wright, N., Sousk, S., Anderson, T., Nguyen, H., Fasulo, J., and Loving, H., Tactical wheeled vehicles and crew survivability in landmine explosions, AMSEL-NV-TR-207, Contermine division, Fort Belvoit, VA 22060, 1998.

[23] Condon, J.A., Gniazdowski, N., and Gregory, F.H., The design, testing, and analysis of a proposed composite hull technology mine-blast-resistant vehicle floor panel, ARL-TR-796, 1995.

[24] Yen, C.-F., and Jones, M.L., Composite material modeling for blast protection, MSC-TFR-3705/CB02, Countermine Division, Fort Belvoir, VA 22060, 1996.